

# Helium abundance in a sample of cool stars: measurements from asteroseismology

Kuldeep Verma,<sup>1\*</sup> Keyuri Raodeo,<sup>2</sup> Sarbani Basu,<sup>3</sup> Víctor Silva Aguirre,<sup>1</sup>  
Anwesh Mazumdar,<sup>2</sup> Jakob Rørsted Mosumgaard,<sup>1</sup> Mikkel N. Lund,<sup>4,1</sup>  
and Pritesh Ranadive<sup>2</sup>

<sup>1</sup>*Stellar Astrophysics Centre, Department of Physics and Astronomy, Aarhus University, Ny Munkegade 120, DK-8000 Aarhus C, Denmark*

<sup>2</sup>*Homi Bhabha Centre for Science Education, TIFR, V. N. Purav Marg, Mankhurd, Mumbai 400088, India*

<sup>3</sup>*Astronomy Department, Yale University, P. O. Box 208101, New Haven, CT 065208101, USA*

<sup>4</sup>*School of Physics and Astronomy, University of Birmingham, Edgbaston, Birmingham, B15 2TT, UK*

Accepted XXX. Received YYY; in original form ZZZ

## ABSTRACT

The structural stratification of a solar-type main sequence star primarily depends on its mass and chemical composition. The surface heavy element abundances of the solar-type stars are reasonably well determined using conventional spectroscopy, however the second most abundant element helium is not. This is due to the fact that the envelope temperature of such stars is not high enough to excite helium. Since the helium abundance of a star affects its structure and subsequent evolution, the uncertainty in the helium abundance of a star makes estimates of its global properties (mass, radius, age etc.) uncertain as well. The detections of the signatures of the acoustic glitches from the precisely measured stellar oscillation frequencies provide an indirect way to estimate the envelope helium content. We use the glitch signature caused by the ionization of helium to determine the envelope helium abundance of 38 stars in the *Kepler* seismic LEGACY sample. Our results confirm that atomic diffusion does indeed take place in solar-type stars. We use the measured surface abundances in combination with the settling predicted by the stellar models to determine the initial abundances. The initial helium and metal mass fractions have subsequently been used to get the preliminary estimates of the primordial helium abundance,  $Y_p = 0.244 \pm 0.019$ , and the galactic enrichment ratio,  $\Delta Y / \Delta Z = 1.226 \pm 0.849$ . Although the current estimates have large errorbars due to the limited sample size, this method holds great promises to determine these parameters precisely in the era of upcoming space missions.

**Key words:** stars: abundances – stars: fundamental parameters – stars: interiors – stars: oscillations – stars: solar-type

## 1 INTRODUCTION

The observed oscillation frequencies of the stars from the *Convection, Rotation and planetary Transits* (CoRoT; Baglin et al. 2009) and *Kepler* (Borucki et al. 2009) space missions are expected to contain enormous amount of information about the stellar interiors (see e.g. Ulrich 1986, 1988; Christensen-Dalsgaard 1988, 2002; Aerts et al. 2010), and have been recently used successfully to study them (e.g. Mathur et al. 2012; Metcalfe et al. 2012, 2014; Silva Aguirre et al. 2013, 2015; Lebreton & Goupil 2014; Verma et al. 2014a; Buldgen et al. 2016a, just to name a few). Unfortunately, the current methods of fitting

the stellar oscillation frequencies (see e.g. Metcalfe et al. 2009; Gruberbauer et al. 2012; Silva Aguirre et al. 2015; Verma et al. 2016; Bellinger et al. 2016) do not exploit the full diagnostic potential of the precisely measured oscillation frequencies due to our poor understanding of the near-surface layers – which introduces a frequency-dependent systematic offset in the model frequencies, known as “surface effect” (see Christensen-Dalsgaard et al. 1988; Kjeldsen et al. 2008; Ball & Gizon 2014) – and consequently some of the stellar parameters are not as tightly constrained as they otherwise would be (see e.g. Nsamba et al. 2018).

The initial helium abundance,  $Y_i$ , is one of the least constrained stellar parameter, and is either determined by assuming a galactic enrichment ratio,  $\Delta Y / \Delta Z$ , from the galactic chemical evolution or by adjusting it to fit the

\* E-mail: kuldeep@phys.au.dk (KV)

spectroscopic and seismic data. There is currently no consensus on the value of  $\Delta Y/\Delta Z$ , and different measurements provide significantly different values, typically in the range 0.8 – 3.0 (see e.g. Ribas et al. 2000a; Lebreton et al. 2001; Peimbert et al. 2002; Jimenez et al. 2003; Balser 2006; Casagrande et al. 2007). Consequently very different relationships between  $Y_i$  and initial metal mass fraction,  $Z_i$ , have been used in the recent past to construct the evolutionary tracks and isochrones: for example, Demarque et al. (2004) uses  $Y_i = 0.23 + 2Z_i$ , Dotter et al. (2008)  $Y_i = 0.245 + 1.54Z_i$ , Marigo et al. (2008)  $Y_i = 0.23 + 2.23Z_i$ , Choi et al. (2016)  $Y_i = 0.249 + 1.5Z_i$  and Hidalgo et al. (2018) uses  $Y_i = 0.247 + 1.31Z_i$ . While determining  $Y_i$  by fitting the observed data seems more plausible, it is known to provide biased estimates (Metcalf et al. 2015), even sub-primordial values for some stars (see e.g. Mathur et al. 2012; Metcalf et al. 2014). Nsamba et al. (in prep.) presents a comprehensive exploration of the systematic uncertainties on stellar parameters arising from the treatment of initial helium abundance in the stellar model grids.

The first and second ionizations of the helium atom leads to a peak in the first adiabatic index,  $\Gamma_1$ , between the two ionization zones, which introduces an oscillatory signature in the oscillation frequency,  $\nu$  (see Gough & Thompson 1988; Vorontsov 1988; Gough 1990; Broomhall et al. 2014; Verma et al. 2014b). The recent detections of this signature in the oscillation frequencies of several main-sequence (see e.g. Mazumdar et al. 2014; Verma et al. 2017) and red-giant (Corsaro et al. 2015) stars open the door for a semi-direct method to estimate the surface helium abundance,  $Y_s$ . The amplitude of the oscillatory signature depends on the amount of the helium present in its ionization zones. The theoretical investigations in the past showed the possibility of determining  $Y_s$  using the amplitude of the helium glitch signature (Basu et al. 2004; Houdek 2004; Monteiro & Thompson 2005). More recently, Verma et al. (2014a) used this method for the first time to determine the  $Y_s$  of a binary system, 16 Cyg A & B (KIC 12069424 and 12069449), observed by the *Kepler* satellite. Our estimates of  $Y_s$  for 16 Cyg A & B were used to constrain their internal structure and derive accurately the global properties (see e.g. Buldgen et al. 2015, 2016a,b).

The amplitudes of the glitch signatures are very small, and require a large set of precisely determined oscillation frequencies to measure them reliably. Recently, Lund et al. (2017) identified a set of main-sequence stars with the highest signal-to-noise (S/N) data from the *Kepler* space mission, and dubbed as the “*Kepler* asteroseismic LEGACY sample”. They computed the oscillation frequencies for each star in the sample, which were then used together with the spectroscopic data by a team of modellers to accurately characterize them (Silva Aguirre et al. 2017). Verma et al. (2017) performed the glitch analysis for all the stars in the LEGACY sample to estimate the locations of the helium ionization zone and the base of the envelope convection zone. In the current work, we extend our earlier analysis on the LEGACY sample to calibrate the observed amplitude of the helium signature against the corresponding amplitude in a set of model frequencies of different  $Y_s$  to determine the envelope helium abundance of the stars. We further infer the initial abundances using the determined surface values and settling

predicted by the stellar models, and derive the galactic enrichment ratio.

The rest of the paper is organized as follows. We define the average amplitude of the helium signature, and describe briefly the methods to obtain it from the oscillation frequencies in Section 2. The input physics of the models used for the calibration and the process to retrieve them are outlined in Section 3. We present the results in Section 4. The conclusions of the paper are summarized in Section 5.

## 2 AMPLITUDE OF THE HELIUM SIGNATURE

The functional form of the helium glitch signature can be obtained using the variational principle (Chandrasekhar 1964) by assuming a Gaussian profile for the  $\Gamma_1$ -peak between the two helium ionization zones (Gough 2002; Houdek & Gough 2007), and can be written as,

$$\delta\nu_{\text{He}} = A_{\text{He}}\nu e^{-8\pi^2\Delta_{\text{He}}^2\nu^2} \sin(4\pi\tau_{\text{He}}\nu + \psi_{\text{He}}), \quad (1)$$

where the parameter  $A_{\text{He}}$  is related to the area under the  $\Gamma_1$ -peak,  $\Delta_{\text{He}}$  is related to the width,  $\tau_{\text{He}}$  is the acoustic depth of the peak and the parameter  $\psi_{\text{He}}$  is a phase constant.

We can see from Eq. 1 that the amplitude depends on the oscillation frequency. Different authors in the literature have used different measures of the amplitude for the calibration. For instance, Miglio et al. (2003) suggested to calibrate the area of the  $\Gamma_1$  depression in the second helium ionization zone, while Houdek & Gough (2007) used the height of the depression for the calibration. In the current interpretation of the helium glitch, they would correspond to the area and height of the peak between the two stages of the helium ionization, and are related to the parameters  $A_{\text{He}}$  and  $A_{\text{He}}/\Delta_{\text{He}}$ , respectively. Monteiro & Thompson (2005) proposed to use the amplitude at a reference frequency ( $A_{\nu_0} = A_{\text{He}}\nu_0 e^{-8\pi^2\Delta_{\text{He}}^2\nu_0^2}$ , where  $\nu_0$  is the reference frequency), whereas Basu et al. (2004) used the amplitude averaged over the observed frequency range for the calibration (see also Verma et al. 2014a). In this work, we used the average amplitude,

$$\begin{aligned} \langle A_{\nu} \rangle &= \frac{\int_{\nu_1}^{\nu_2} A_{\text{He}}\nu e^{-8\pi^2\Delta_{\text{He}}^2\nu^2} d\nu}{\int_{\nu_1}^{\nu_2} d\nu} \\ &= \frac{A_{\text{He}}[e^{-8\pi^2\Delta_{\text{He}}^2\nu_1^2} - e^{-8\pi^2\Delta_{\text{He}}^2\nu_2^2}]}{16\pi^2\Delta_{\text{He}}^2[\nu_2 - \nu_1]}, \end{aligned} \quad (2)$$

where  $\nu_1$  and  $\nu_2$  are the smallest and largest observed frequencies used in the fit (the same  $\nu_1$  and  $\nu_2$  are consistently used to calculate model  $\langle A_{\nu} \rangle$ ). We shall discuss the advantage of using  $\langle A_{\nu} \rangle$  for the calibration in the Appendix A.

The extraction of the low-amplitude glitch signatures from the oscillation frequency involves non-linear optimization. To test the convergence of the fitting method, and the robustness of the final estimate of  $Y_s$ , we extracted the helium glitch signature using two different methods. The first (Method A) fitted the oscillation frequencies directly (see Monteiro et al. 1994; Monteiro & Thompson 1998; Monteiro et al. 2000; Verma et al. 2014a), while the second (Method B) fitted the second differences of the oscillation frequencies with respect to the radial order,  $\delta^2\nu_{n,l} = \nu_{n-1,l} - 2\nu_{n,l} + \nu_{n+1,l}$ , where  $n$  and  $l$  are the radial order and

**Table 1.** A summary of the input physics used in the different sets of calibration models.

Model	Opacity	Equation of state	Solar metallicity mixture	Nuclear reaction rates	Diffusion	Overshoot	Frequencies
MESA	OP05+Ferg05	OPAL05	GS98	NACRE	Thoul94	Herwig00	ADIPLS
GARSTEC	OPAL96+Ferg05	OPAL05	GS98	NACRE	–	Freytag96	ADIPLS
YREC	OPAL96+Ferg05	OPAL05	GS98	Adel98	Thoul94	Maeder75	Antia94

References: OP05 (Badnell et al. 2005; Seaton 2005), OPAL96 (Iglesias & Rogers 1996), Ferg05 (Ferguson et al. 2005), OPAL05 (2005 version of Rogers & Nayfonov 2002), GS98 (Grevesse & Sauval 1998), NACRE (Angulo et al. 1999), Adel98 (Adelberger et al. 1998), Thoul94 (Thoul et al. 1994), Herwig00 (Herwig 2000), Freytag96 (Freytag et al. 1996), Maeder75 (Maeder 1975), ADIPLS (Christensen-Dalsgaard 2008), Antia94 (Antia & Basu 1994)

harmonic degree, respectively (see Gough 1990; Basu et al. 1994, 2004; Verma et al. 2014a). The details of the methods used in the current work had been described in Verma et al. (2014a). Here, we only outline them for the reader and highlight the minor differences from the previous works.

### 2.1 Fitting the frequencies directly (Method A)

We modelled the smooth component of the oscillation frequencies corresponding to the smooth structure of the star using a  $l$ -dependent fourth degree polynomial in  $n$ ,

$$\nu_{\text{smooth}}(n, l) = \sum_{k=0}^4 b_k(l) n^k. \quad (3)$$

The degree dependence of the polynomial coefficients,  $b_k(l)$ , simply means that they are different for the different  $l$ , and need to be determined. We determined these coefficients together with the parameters associated with the glitch signatures – including  $A_{\text{He}}$  and  $\Delta_{\text{He}}$  required for the average amplitude – by fitting the oscillation frequencies to the function,

$$f(n, l) = \nu_{\text{smooth}} + \delta\nu_{\text{He}} + \delta\nu_{\text{CZ}}, \quad (4)$$

where  $\delta\nu_{\text{CZ}} = \frac{A_{\text{CZ}}}{\nu^2} \sin(4\pi\tau_{\text{CZ}}\nu + \psi_{\text{CZ}})$  is the glitch signature arising from the base of the envelope convection zone. The parameter  $A_{\text{CZ}}$  is related to the jump in the second derivative of the sound speed at the base of the convection zone,  $\tau_{\text{CZ}}$  is the acoustic depth of the convection zone base and  $\psi_{\text{CZ}}$  is a phase constant.

The fitting was accomplished by minimizing a cost function,

$$\chi_{\text{A}}^2 = \sum_{n,l} \left[ \frac{\nu_{n,l} - f(n,l)}{\sigma_{n,l}} \right]^2 + \lambda_{\text{A}}^2 \sum_{n,l} \left[ \frac{d^3\nu_{\text{smooth}}}{dn^3} \right]^2, \quad (5)$$

where  $\sigma_{n,l}$  is the uncertainty on  $\nu_{n,l}$  and  $\lambda_{\text{A}}$  a regularization parameter. Note that the third derivative regularization used in this work (also used in Verma et al. 2017) marginally improves the stability of the fit in comparison to the second derivative used in Verma et al. (2014a,b). Previous work has shown that  $\lambda_{\text{A}} = 7$  is a suitable choice (Verma et al. 2017). While fitting the models we used the same set of modes and weights as for the observations. We propagated the statistical uncertainties on the observed oscillation frequencies to the glitch parameters by fitting 1000 realizations of the data (Monte-Carlo simulation). The model frequencies do not have statistical uncertainties, however they are known to be affected by the systematic uncertainties because of the uncertainties in the stellar and modal physics. A combination of these uncertainties show up as surface effect. We shall quantify the impact of the surface term on the glitch

parameters in the Appendix B, and show that its effect is small.

### 2.2 Fitting the second differences (Method B)

Motivated from the asymptotic theory of the stellar oscillations (Tassoul 1980) we assumed that the smooth component of the second differences is independent of  $l$ , and modelled it with a quadratic function of the frequency,  $\delta^2\nu_{\text{smooth}} = a_0 + a_1\nu + a_2\nu^2$ . In this method, the glitch parameters were determined by fitting the second differences of the oscillation frequencies to the function,

$$g(n, l) = \delta^2\nu_{\text{smooth}} + a_{\text{He}}\nu e^{-8\pi^2\Delta_{\text{He}}^2\nu^2} \sin(4\pi\tau_{\text{He}}\nu + \phi_{\text{He}}) + \frac{a_{\text{CZ}}}{\nu^2} \sin(4\pi\tau_{\text{CZ}}\nu + \phi_{\text{CZ}}), \quad (6)$$

where the second and third term represent the helium and convection zone signature, respectively. Note that the amplitudes,  $a_{\text{He}}$  and  $a_{\text{CZ}}$ , and the phases,  $\phi_{\text{He}}$  and  $\phi_{\text{CZ}}$ , of the signatures in the second differences are different from the corresponding amplitudes and phases of the signatures in the oscillation frequencies (see Eq. 4). The amplitude of the helium signature in the second differences is related to the amplitude in the frequencies,  $a_{\text{He}} \approx 4A_{\text{He}} \sin^2(2\pi\tau_{\text{He}}\langle\Delta\nu\rangle)$ , where  $\langle\Delta\nu\rangle$  is the average large frequency separation (see Basu et al. 1994).

We determined  $a_0$ ,  $a_1$ ,  $a_2$  and the glitch parameters by minimizing a cost function,

$$\chi_{\text{B}}^2 = \mathbf{x}^T \mathbf{C}^{-1} \mathbf{x} + \lambda_{\text{B}}^2 \sum_{n,l} \left[ \frac{d\delta^2\nu_{\text{smooth}}}{d\nu} \right]^2, \quad (7)$$

where  $\mathbf{x}$  is a vector containing the differences between the observed and model second differences,  $\mathbf{C}$  the analytic covariance matrix for the second differences and  $\lambda_{\text{B}}$  is a regularization parameter. In this method, the choice of the degree of polynomial for the smooth component and the order of derivative in the regularization term are both inspired by Method A. Since we are fitting the second difference of the oscillation frequency, the degree of polynomial and the order of derivative were both reduced by two to second degree polynomial and first order derivative. We used the data for 16 Cyg A & B and followed the procedure described in Verma et al. (2014a) to find an optimal value of  $\lambda_{\text{B}} = 1000$ . Again, the same set of modes and weights were used while fitting the model frequencies. We propagated the observational uncertainties on the oscillation frequencies to the glitch parameters using the Monte-Carlo simulation.

**Table 2.** The initial parameter space covered by the MESA and YREC (non-diffusion set) for each star. The solar calibrated mixing-length for the MESA and YREC with the input physics described in Section 3 are 1.91 (1.84 when excluding the atomic diffusion) and 1.70, respectively. The missing range for  $f_{\text{OV}}$  for some stars means that the overshoot was not included. For the YREC,  $\alpha_{\text{OV}}$  was fixed at  $0.2H_p$ , where  $H_p$  is the pressure scale height.

KIC	MESA					YREC				
	$M$ ( $M_{\odot}$ )	$Y_i$	$[\text{Fe}/\text{H}]_i$	$\alpha_{\text{MLT}}$	$f_{\text{OV}}$	$M$ ( $M_{\odot}$ )	$Y_i$	$[\text{Fe}/\text{H}]_i$	$\alpha_{\text{MLT}}$	
1435467	1.25–1.55	0.22–0.32	−0.10 – +0.10	1.5–2.0	0.00–0.03	1.30–1.55	0.16–0.34	−0.10 – +0.25	1.60–2.10	
2837475	1.30–1.60	0.22–0.32	−0.10 – +0.10	1.5–2.0	0.00–0.03	1.40–1.90	0.05–0.32	−0.08 – +0.18	1.65–1.90	
3427720	1.00–1.30	0.22–0.32	−0.05 – +0.15	1.5–2.0	0.00–0.03	1.05–1.40	0.10–0.28	−0.15 – +0.05	1.50–2.10	
3456181	1.35–1.65	0.22–0.32	−0.25 – −0.05	1.5–2.0	0.00–0.03	1.40–1.80	0.10–0.28	−0.20 – +0.00	1.60–2.10	
3632418	1.05–1.35	0.22–0.32	−0.10 – +0.10	1.5–2.0	0.00–0.05	1.30–1.55	0.12–0.28	−0.20 – +0.10	1.40–1.95	
3656476	1.00–1.30	0.24–0.34	+0.30 – +0.50	1.5–2.0	0.00–0.03	1.02–1.20	0.20–0.30	+0.05 – +0.35	1.45–1.90	
3735871	1.00–1.30	0.22–0.32	−0.10 – +0.10	1.5–2.0	0.00–0.03	1.05–1.35	0.12–0.30	−0.15 – +0.05	1.50–2.10	
4914923	1.00–1.30	0.22–0.32	+0.15 – +0.35	1.5–2.0	0.00–0.03	0.96–1.22	0.16–0.32	−0.10 – +0.30	1.20–1.90	
5184732	1.05–1.35	0.24–0.34	+0.35 – +0.55	1.5–2.0	0.00–0.03	1.15–1.50	0.15–0.34	+0.15 – +0.45	1.45–1.90	
5773345	1.30–1.60	0.22–0.32	+0.10 – +0.30	1.5–2.0	0.00–0.03	1.45–1.80	0.12–0.32	+0.10 – +0.40	1.40–2.10	
5950854	0.80–1.10	0.22–0.32	−0.20 – +0.00	1.5–2.0	...	0.95–1.20	0.06–0.26	−0.40 – −0.05	1.40–2.10	
6106415	0.95–1.25	0.22–0.32	−0.10 – +0.10	1.5–2.0	...	1.06–1.24	0.18–0.27	−0.20 – +0.05	1.55–1.90	
6116048	0.95–1.25	0.20–0.30	−0.20 – +0.00	1.5–2.0	...	1.00–1.20	0.13–0.26	−0.40 – −0.05	1.45–1.90	
6225718	1.00–1.30	0.22–0.32	−0.15 – +0.05	1.5–2.0	0.00–0.05	1.15–1.45	0.14–0.28	−0.20 – +0.05	1.60–2.10	
6508366	1.35–1.65	0.22–0.32	−0.15 – +0.05	1.5–2.0	0.00–0.03	1.45–1.80	0.10–0.30	−0.10 – +0.10	1.65–1.90	
6603624	0.90–1.20	0.22–0.32	+0.25 – +0.45	1.5–2.0	...	0.95–1.20	0.16–0.30	−0.00 – +0.35	1.40–2.10	
6679371	1.35–1.65	0.22–0.32	−0.10 – +0.10	1.5–2.0	0.00–0.03	1.40–1.65	0.24–0.34	−0.10 – +0.20	1.45–1.90	
6933899	1.00–1.30	0.22–0.32	+0.05 – +0.25	1.5–2.0	0.00–0.03	1.05–1.30	0.14–0.28	−0.15 – +0.10	1.25–1.50	
7103006	1.15–1.35	0.22–0.32	+0.05 – +0.25	1.5–2.0	0.00–0.03	1.30–1.75	0.10–0.35	−0.10 – +0.20	1.65–1.90	
7106245	0.70–1.00	0.22–0.32	−0.85 – −0.55	1.5–2.0	...	0.90–1.15	0.06–0.26	−0.90 – −0.45	1.20–2.00	
7206837	1.25–1.55	0.22–0.32	+0.05 – +0.25	1.5–2.0	0.00–0.05	1.25–1.65	0.10–0.35	−0.00 – +0.25	1.45–1.90	
7296438	1.00–1.30	0.22–0.32	+0.20 – +0.40	1.5–2.0	0.00–0.03	1.05–1.30	0.16–0.30	+0.05 – +0.35	1.45–1.90	
7510397	1.15–1.40	0.22–0.32	−0.15 – +0.15	1.5–2.0	0.00–0.05	1.30–1.50	0.14–0.32	−0.30 – +0.10	1.40–1.90	
7680114	1.00–1.30	0.22–0.32	+0.10 – +0.30	1.5–2.0	0.00–0.03	1.05–1.25	0.16–0.28	−0.10 – +0.15	1.40–1.90	
7771282	1.15–1.35	0.22–0.32	+0.00 – +0.20	1.5–2.0	0.00–0.03	1.20–1.55	0.16–0.32	−0.10 – +0.10	1.60–1.90	
7871531	0.70–1.00	0.22–0.32	−0.25 – +0.05	1.5–2.0	...	0.80–1.05	0.08–0.30	−0.35 – −0.10	1.50–2.10	
7940546	1.20–1.40	0.22–0.32	−0.05 – +0.15	1.5–2.0	0.00–0.03	1.35–1.55	0.10–0.30	−0.30 – +0.05	1.40–1.90	
7970740	0.65–0.95	0.22–0.32	−0.50 – −0.20	1.5–2.0	...	0.70–0.90	0.10–0.28	−0.70 – −0.35	1.40–2.10	
8006161	0.80–1.10	0.22–0.32	+0.30 – +0.50	1.5–2.0	...	0.90–1.10	0.22–0.33	+0.15 – +0.45	1.60–2.10	
8150065	1.00–1.30	0.22–0.32	−0.10 – +0.10	1.5–2.0	0.00–0.03	1.10–1.70	0.05–0.30	−0.20 – +0.05	1.40–1.90	
8179536	1.15–1.35	0.22–0.32	+0.00 – +0.20	1.5–2.0	0.00–0.03	1.20–1.70	0.05–0.32	−0.10 – +0.10	1.60–2.10	
8228742	1.05–1.35	0.20–0.30	−0.05 – +0.15	1.5–2.0	0.00–0.03	1.30–1.50	0.16–0.30	−0.20 – +0.05	1.45–1.90	
8379927	1.00–1.30	0.20–0.30	−0.20 – +0.00	1.5–2.0	0.00–0.05	1.10–1.30	0.14–0.30	−0.30 – +0.30	1.40–2.10	
8394589	0.90–1.20	0.22–0.32	−0.30 – −0.10	1.5–2.0	...	1.00–1.20	0.15–0.28	−0.40 – −0.15	1.45–1.70	
8424992	0.70–1.00	0.22–0.32	−0.10 – +0.10	1.5–2.0	...	0.90–1.10	0.10–0.30	−0.30 – +0.10	1.60–2.10	
8694723	0.95–1.25	0.20–0.30	−0.45 – −0.15	1.5–2.0	0.00–0.03	1.10–1.30	0.18–0.23	−0.50 – −0.20	1.40–1.90	
8760414	0.70–1.00	0.20–0.30	−1.05 – −0.60	1.5–2.0	...	0.80–0.91	0.14–0.25	−1.05 – −0.55	1.30–1.90	
8938364	0.80–1.10	0.22–0.32	−0.15 – +0.15	1.5–2.0	...	0.90–1.10	0.20–0.29	−0.30 – +0.10	1.20–1.70	
9025370	0.75–1.05	0.22–0.32	−0.10 – +0.10	1.5–2.0	...	0.90–1.25	0.05–0.32	−0.20 – +0.20	1.20–1.70	
9098294	0.85–1.15	0.22–0.32	−0.18 – +0.02	1.5–2.0	...	0.98–1.12	0.14–0.28	−0.30 – +0.05	1.60–1.90	
9139151	1.00–1.30	0.22–0.32	+0.05 – +0.25	1.5–2.0	0.00–0.05	1.10–1.35	0.16–0.32	−0.10 – +0.20	1.80–2.30	
9139163	1.30–1.60	0.22–0.32	+0.05 – +0.25	1.5–2.0	0.00–0.03	1.30–1.70	0.15–0.35	−0.00 – +0.40	1.60–2.10	
9206432	1.35–1.65	0.22–0.32	+0.05 – +0.25	1.5–2.0	0.00–0.03	1.30–2.00	0.10–0.34	+0.10 – +0.35	1.80–2.10	
9353712	1.25–1.55	0.22–0.32	−0.15 – +0.05	1.5–2.0	0.00–0.03	1.45–1.70	0.16–0.30	+0.15 – +0.15	1.60–1.90	
9410862	0.80–1.10	0.22–0.32	−0.30 – −0.10	1.5–2.0	...	0.95–1.10	0.16–0.30	−0.45 – −0.15	1.45–1.90	
9414417	1.10–1.30	0.22–0.32	−0.10 – +0.10	1.5–2.0	0.00–0.03	1.35–1.70	0.05–0.30	−0.25 – +0.05	1.65–1.80	
9812850	1.15–1.35	0.22–0.32	−0.05 – +0.15	1.5–2.0	0.00–0.03	1.30–1.70	0.10–0.30	−0.20 – +0.10	1.60–2.10	
9955598	0.70–1.00	0.22–0.32	+0.10 – +0.30	1.5–2.0	...	0.85–1.05	0.16–0.30	−0.10 – +0.25	1.60–2.10	
9965715	0.80–1.10	0.22–0.32	−0.35 – −0.05	1.5–2.0	...	1.00–1.40	0.00–0.28	−0.55 – −0.10	1.20–1.70	
10068307	1.20–1.40	0.22–0.32	−0.15 – +0.05	1.5–2.0	0.00–0.03	1.40–1.75	0.05–0.28	−0.30 – +0.10	1.20–2.00	
10079226	1.00–1.30	0.22–0.32	+0.05 – +0.25	1.5–2.0	0.00–0.03	1.05–1.30	0.16–0.32	−0.00 – +0.20	1.40–1.90	
10162436	1.05–1.40	0.22–0.32	−0.05 – +0.15	1.5–2.0	0.00–0.05	1.35–1.60	0.14–0.30	−0.20 – +0.10	1.40–1.90	
10454113	1.00–1.30	0.22–0.32	−0.05 – +0.15	1.5–2.0	0.00–0.05	1.10–1.40	0.12–0.30	−0.10 – +0.10	1.40–1.70	
10516096	1.00–1.30	0.22–0.32	−0.10 – +0.10	1.5–2.0	0.00–0.03	1.05–1.25	0.15–0.26	−0.25 – +0.00	1.40–1.90	
10644253	1.00–1.30	0.22–0.32	+0.10 – +0.30	1.5–2.0	0.00–0.03	1.05–1.35	0.16–0.30	−0.05 – +0.20	1.45–1.90	
10730618	1.15–1.35	0.22–0.32	−0.10 – +0.10	1.5–2.0	0.00–0.03	1.20–1.60	0.05–0.33	−0.20 – +0.25	1.20–2.10	
10963065	0.90–1.20	0.22–0.32	−0.15 – +0.05	1.5–2.0	...	1.00–1.20	0.16–0.28	−0.35 – −0.10	1.45–1.75	
11081729	1.20–1.40	0.22–0.32	+0.15 – +0.35	1.5–2.0	0.00–0.03	1.20–1.60	0.12–0.34	−0.00 – +0.25	1.80–2.20	
11253226	1.30–1.60	0.22–0.32	−0.20 – +0.00	1.5–2.0	0.00–0.03	1.30–1.90	0.00–0.33	−0.15 – +0.15	1.65–2.10	
11772920	0.70–1.00	0.22–0.32	−0.10 – +0.10	1.5–2.0	...	0.80–1.05	0.00–0.30	−0.30 – +0.20	1.40–2.10	
12009504	1.00–1.30	0.22–0.32	−0.05 – +0.15	1.5–2.0	0.00–0.03	1.15–1.45	0.08–0.32	−0.25 – +0.10	1.40–2.10	
12069127	1.35–1.65	0.22–0.32	+0.00 – +0.20	1.5–2.0	0.00–0.03	1.45–1.85	0.14–0.32	−0.00 – +0.20	1.60–1.90	
12069424	0.85–1.15	0.22–0.32	+0.10 – +0.30	1.5–2.0	...	1.00–1.20	0.20–0.27	+0.02 – +0.16	1.55–1.90	
12069449	0.85–1.15	0.22–0.32	+0.05 – +0.25	1.5–2.0	...	0.95–1.15	0.19–0.31	−0.00 – +0.20	1.50–2.10	
12258514	1.00–1.30	0.22–0.32	+0.05 – +0.25	1.5–2.0	0.00–0.05	1.20–1.45	0.10–0.28	−0.10 – +0.15	1.40–2.00	
12317678	1.10–1.30	0.22–0.32	−0.15 – +0.05	1.5–2.0	0.00–0.03	1.20–1.70	0.05–0.32	−0.40 – −0.10	1.65–2.10	



### 3 CALIBRATION MODELS

We used four different sets of the calibration models: one with the Modules for Experiments in Stellar Astrophysics (MESA; Paxton et al. 2011, 2013), one with the Garching Stellar Evolution Code (GARSTEC; Weiss & Schlattl 2008) and two with the Yale Rotating Stellar Evolution Code (YREC; Demarque et al. 2008). This was done to quantify the systematic uncertainties on inferred  $Y_s$  associated with the choice of the input physics. A summary of the input physics used in these codes is provided in Table 1. The second set of the YREC models use the same input physics as the one in the table, except that it does not include atomic diffusion. The details of the input physics and the procedure to get the calibration models are described below for all the sets.

#### 3.1 MESA models

We used MESA with Opacity Project (OP) high-temperature opacities (Badnell et al. 2005; Seaton 2005) supplemented with low-temperature opacities of Ferguson et al. (2005). The metallicity mixture from Grevesse & Sauval (1998) was used. We used OPAL equation of state (Rogers & Nayfonov 2002). The reaction rates were from NACRE (Angulo et al. 1999) for all reactions except  $^{14}\text{N}(p, \gamma)^{15}\text{O}$  and  $^{12}\text{C}(\alpha, \gamma)^{16}\text{O}$ , for which updated reaction rates from Imbriani et al. (2005) and Kunz et al. (2002) were used. Since the inclusion of atomic diffusion leads to complete depletion of the surface helium and heavy elements for solar metallicity stellar models of masses approximately greater than  $1.4 M_\odot$  (see e.g. Morel & Thévenin 2002), we included this process only for the stars of masses less than  $1.35 M_\odot$  using the prescription of Thoul et al. (1994). It is now well known that the stars with masses approximately greater than  $1.1 M_\odot$  have finite convective core overshoot (see e.g. Deheuvels et al. 2010; de Meulenaer et al. 2010; Silva Aguirre et al. 2013), though the value of the overshoot parameter remains uncertain, and may depend on the mass of the star (see e.g. Ribas et al. 2000b; Claret & Torres 2016). Hence we used an exponential overshoot (Herwig 2000) with variable overshoot parameter,  $f_{\text{OV}}$ , for the stars with masses greater than  $1.10 M_\odot$ . The adiabatic oscillation frequencies were calculated using the Adiabatic Pulsation code (ADIPLS; Christensen-Dalsgaard 2008).

In this approach of constructing the calibration models, the choice of input physics depends on the mass of the star at hand. We estimate the mass using the asteroseismic scaling relations (Kjeldsen & Bedding 1995), and use the input physics based on that. The detailed asteroseismic modelling of the star eventually provides more accurate value of the mass. We restart the process if the new mass suggests that the input physics needs to be changed. This is rare but may happen if the mass of the star is close to either  $1.10$  or  $1.35 M_\odot$ .

We computed the tracks for each star with different mass  $M$ , initial helium abundance  $Y_i$ , initial metallicity  $[\text{Fe}/\text{H}]_i$ , mixing-length  $\alpha_{\text{MLT}}$  and overshoot parameter  $f_{\text{OV}}$ . We generated 1000–2000 mesh points randomly with uniform distribution in the parameter space listed in Table 2. The initial parameter ranges listed in the table were iteratively

modified so that the best-fitting model did not fall at the edge of the parameter space.

We evolved the initial pre-main-sequence model corresponding to every mesh point until the track entered in a box formed by the  $4\sigma$  uncertainties in the observed effective temperature  $T_{\text{eff}}$ , surface metallicity  $[\text{Fe}/\text{H}]_s$  and the average large frequency separation  $\langle \Delta\nu \rangle$ . Afterwards, we fitted the surface corrected model frequencies (Kjeldsen et al. 2008) on the fly to the observed ones to break the degeneracy inside the box, and accept the best-fitting model as a representative model of the concerned star. Repeating the above process for all the mesh points, we got a set of approximately 1000–2000 representative models for each star.

The choice of the surface correction scheme is not important in this particular exercise because, for a given initial condition ( $M$ ,  $Y_i$ ,  $[\text{Fe}/\text{H}]_i$ ,  $\alpha_{\text{MLT}}$  and  $f_{\text{OV}}$ ), the age can be determined very precisely by fitting the observed oscillation frequencies irrespective of the surface correction used. The large uncertainties in the inferred ages of the stars are the result of the uncertainties in the initial conditions, particularly in  $M$  and  $f_{\text{OV}}$ . Having said that, the YREC models use a different surface correction (Ball & Gizon 2014, see Section 3.3), and hence its impact can be estimated by comparing the  $Y_s$  from the MESA/GARSTEC and YREC.

#### 3.2 GARSTEC models

The code was used with OPAL high-temperature opacities (Iglesias & Rogers 1996) supplemented with low-temperature opacities of Ferguson et al. (2005). We used solar metallicity mixture from Grevesse & Sauval (1998). The OPAL equation of state was used (Rogers & Nayfonov 2002). All the reaction rates were from NACRE except  $^{14}\text{N}(p, \gamma)^{15}\text{O}$  and  $^{12}\text{C}(\alpha, \gamma)^{16}\text{O}$  for which the rates from Formicola et al. (2004) and Hammer et al. (2005) were used. We did not include atomic diffusion in this case intentionally to formally incorporate the associated systematic uncertainty on the quoted values of  $Y_s$ . The overshoot was included for all the stars following the prescription of Freytag et al. (1996) with variable overshoot parameter,  $f_{\text{OV}}$ . Note that the expression for the overshoot diffusion coefficient is same for both Freytag et al. (1996) and Herwig (2000), and hence the same associated overshoot parameter. Aarhus adiabatic pulsation package (ADIPLS) was used for the frequency calculations (Christensen-Dalsgaard 2008).

We generated 6000 tracks in the parameter space  $M \in [0.7, 1.8] M_\odot$ ,  $Y_i \in [0.15, 0.40]$ ,  $[\text{Fe}/\text{H}]_i \in [-1.2, 0.6]$  dex,  $\alpha_{\text{MLT}} \in [1.5, 2.2]$  and  $f_{\text{OV}} \in [0.00, 0.03]$ . The above space was again populated randomly from uniform distribution, but this time using quasi-random number generator (Sobol 1967) instead of pseudo-random number. We stored every third model during the evolution, resulting several hundred main-sequence models per track. Note that this way of generating a grid is slightly different from the ones generated using MESA, for which the initial parameter space is limited to a target star (particularly the mass and initial metallicity) and only one model – that fits the observed frequencies the best – is stored per track. The increased parameter space and storing several hundred to a thousand models per track for GARSTEC increase the grid size considerably. The advantage of one such giant grid is that we can reuse it for the newly observed stars unlike the grid constructed using

the MESA. The disadvantage is that we need much larger disk space (current grid needs 4TBs of disk space to store the local properties of the models needed for the frequency computation). Furthermore, the models on a track have poorer temporal resolution.

We obtained models for the individual stars from the above tracks following the same procedure as for the MESA, i.e. we scanned all the models in a track and located the age range where  $T_{\text{eff}}$ ,  $[\text{Fe}/\text{H}]_s$  and  $\langle\Delta\nu\rangle$  were all within  $4\sigma$  of the observed values, subsequently we fitted the surface corrected model frequencies (Kjeldsen et al. 2008) to get a representative model for the star. Repeating this for all the 6000 tracks, we obtain several tens to few hundred models per star.

### 3.3 YREC models

We used YREC with OPAL high-temperature opacities (Iglesias & Rogers 1996) supplemented with low-temperature opacities of Ferguson et al. (2005). The metallicity mixture from Grevesse & Sauval (1998) was used. We used the 2005 version of the OPAL equation of state (Rogers & Nayfonov 2002). All the nuclear reaction rates were from Adelberger et al. (1998) except for the  $^{14}\text{N}(p,\gamma)^{15}\text{O}$  reaction, for which we used the updated rates of Formicola et al. (2004). A step overshoot (Maeder 1975) of  $\alpha_{\text{OV}} = 0.2H_p$ , where  $H_p$  is the pressure scale height, was used for all the stars. The YREC models were used to isolate the impact of the atomic diffusion on  $Y_s$  determination by using the models with and without diffusion. The adiabatic oscillation frequencies were calculated using a code described in Antia & Basu (1994).

The Yale Monte-Carlo Method (YMCM; Silva Aguirre et al. 2015) was used to get a set of representative models for each star. We started with using the average large frequency separation and frequency of maximum power along with the spectroscopically determined effective temperature to get an estimate of the mass and radius of the star using the Yale Birmingham Grid-Based modelling pipeline (Basu et al. 2010; Gai et al. 2011). Since each of the observables has the associated observational error, we created thousands of realizations of  $M$ ,  $R$ ,  $T_{\text{eff}}$ , and  $[\text{Fe}/\text{H}]_s$ . For each realization, we used the YREC in an iterative mode to obtain a model of given  $M$  and  $[\text{Fe}/\text{H}]_s$  that had the required  $R$  and  $T_{\text{eff}}$ . This was done in two different ways: in the first approach, we kept  $\alpha_{\text{MLT}}$  fixed at different values and iterated over  $Y_i$  to get the model; and in the second approach, we kept  $Y_i$  fixed at different values and varied  $\alpha_{\text{MLT}}$  to get the required model. Finally, a set of representative models of the star was obtained based on the merit function,

$$\chi_{\text{total}}^2 = \chi_{\nu}^2 + \chi_{\text{ratios}}^2 + \chi_{\text{Teff}}^2 + \chi_{[\text{Fe}/\text{H}]_s}^2, \quad (8)$$

where  $\chi_{\nu}^2$  and  $\chi_{\text{ratios}}^2$  are the reduced chi-squares for the oscillation frequencies and frequency ratios,  $r_{02}$  and  $r_{01}$  (for the definition of ratios, see Roxburgh & Vorontsov 2003). The  $\chi_{\nu}^2$  was computed using the surface corrected model frequencies (two term correction of Ball & Gizon 2014). Since ratios are independent of the surface term and are strongly correlated, the  $\chi_{\text{ratios}}^2$  was calculated using the uncorrected model frequencies and using full error covariance matrix.

In this case, the ranges in  $M$ ,  $Y_i$ ,  $[\text{Fe}/\text{H}]_i$  and  $\alpha_{\text{MLT}}$  are

result of the above process, and are listed in Table 2 for only the non-diffusion set.

## 4 RESULTS

We fitted the signatures of the acoustic glitches in all the sets of uncorrected model frequencies (MESA, GARSTEC and YREC) using the both fitting methods (A and B). The fits were subsequently used to compute the average amplitude using Eq. 2.

### 4.1 Final set of models used in the calibration

We filter all the sets of models from Section 3 homogeneously using the frequency ratios. Note that this does not affect the sets of YREC models much, because Eq. 8 already used the ratios. The process of filtering is illustrated in Figure 1. We can see in the top panel that the average amplitude increases as a function of  $Y_s$ , as expected. However, there is a large vertical spread due to the spread in the mass, as revealed by the colour coding. This is also expected, as  $\langle A_{\nu} \rangle$  is known to depend on  $Y_s$  as well as on  $M$  (Verma et al. 2014b). To filter out the models with extreme masses, we defined a cost function,

$$\chi^2 = \chi_{\text{Teff}}^2 + \chi_{[\text{Fe}/\text{H}]_s}^2 + \chi_{02}^2 + \chi_{01}^2 + \chi_{10}^2, \quad (9)$$

where the last three terms are the reduced chi-squares for the different frequency ratios computed using their covariance matrices. The covariances were calculated using 10000 realizations of the observed oscillation frequencies. We would ideally expect the  $\chi^2$  to be close to 5 for the best-fitting models of the stars.

We can see from the middle panel of Figure 1 that the models with the extreme masses on the top and bottom have very large values of  $\chi^2$  (note the logarithmic scale). Such models do not represent 16 Cyg A, and should either be dropped or given less weight while fitting the straight line for the calibration. We do both: the models with  $\chi^2$  greater than a threshold are dropped first, and then a straight-line is fitted to the remaining models with the weight of  $e^{-\chi^2/5}$ . We wish to point out that the threshold on  $\chi^2$  is not important for  $Y_s$  determination because of the exponential weighting, and is applied only to see the correlation clearly. Note that this process of filtering is slightly different from that used in Verma et al. (2014a), where we first determined the age using the spectroscopic and seismic data, and then filtered the models that had age within  $1\sigma$  of the determined value. The filtering method used in the current analysis is more generic – using only the observables – and is less model dependent. As we shall see in Section 4.2, the surface helium abundances found in the current work for 16 Cyg A & B are in good agreement with the values obtained by Verma et al. (2014a).

Figure 2 shows four calibration diagrams for 16 Cyg A obtained using the Methods A and B and the models MESA and GARSTEC. We can see that the two columns look very similar meaning that the extraction of the glitch signature is insensitive to the method used. Figure 2 can be used to get four estimates of  $Y_s$  for 16 Cyg A. Note in the figure that, to determine the surface helium abundance of a star reliably, we need (1) a precise enough determination of the

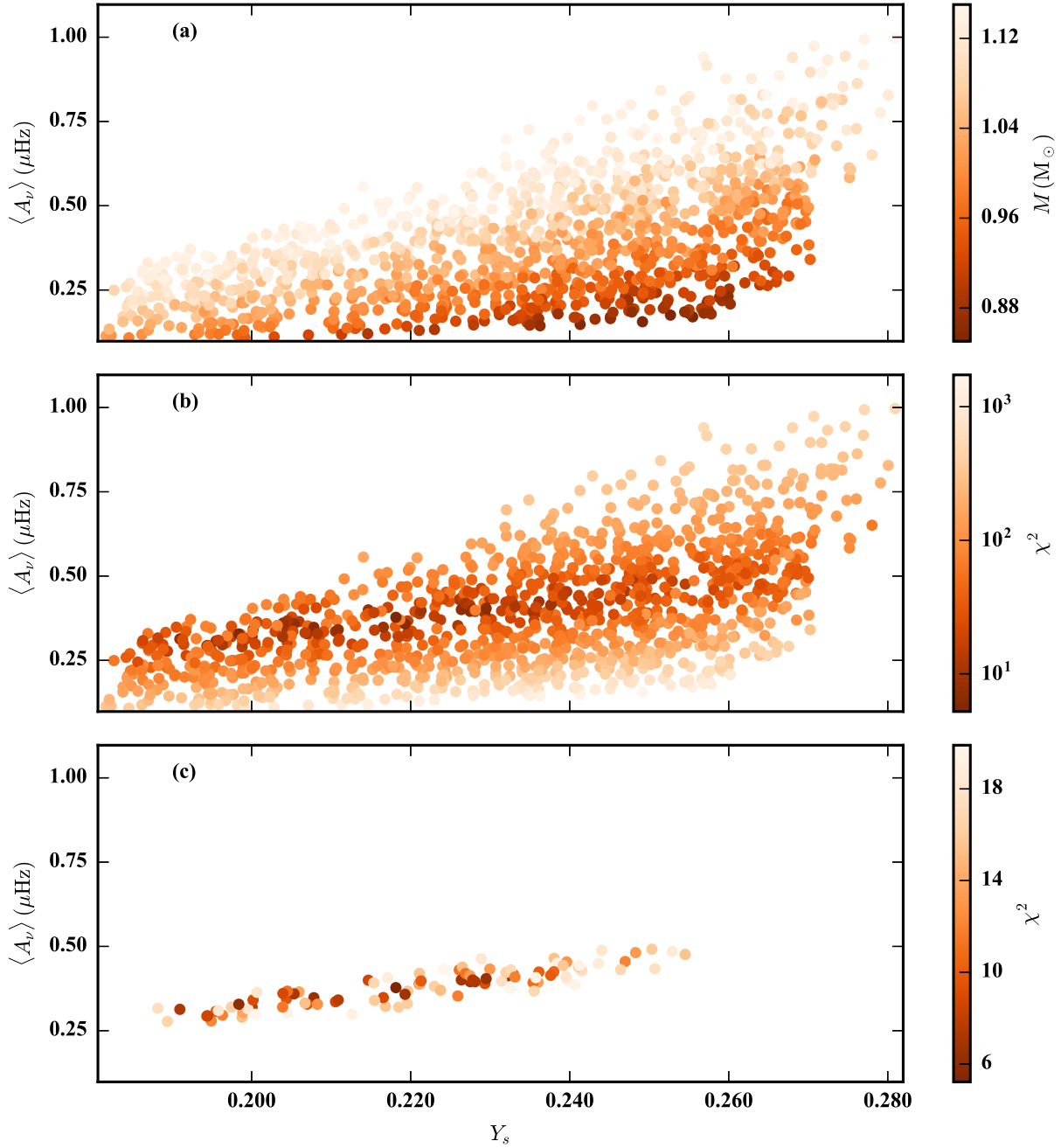


**Figure 1.** Average amplitude of the helium glitch signature obtained using Method A for the models of 16 Cyg A as a function of the envelope helium abundance. The points in the panels (a–b) represent all the models obtained using MESA. The points in the panel (c) represent the models with  $\chi^2$  (as defined in Eq. 9) less than 20. The colour in the panel (a) shows the mass of the models, while in the panels (b–c) it represents their  $\chi^2$  value.

observed  $\langle A_\nu \rangle$ , and (2) a reasonably tight correlation. We have 38 stars in the LEGACY sample for which both the requirements are met. Unfortunately, there is no straightforward way to relate the above two requirements with the quality of the observations. Having said that, Figure 3 makes an attempt to explain why the rest of the 28 stars from the LEGACY sample are rejected.

The precision of the observed  $\langle A_\nu \rangle$  not only depends on the precision of the observed oscillation frequencies, but also on the number of modes detected and on the mass

of the star. The mass dependence is due to the fact that the strength of the helium glitch signature depends on the mass – the larger the mass, the stronger the signature – making it easier to detect (Verma et al. 2014b). Typically, the observed power spectrum of a low-mass star has poor S/N, and hence the number of detected modes are limited (see Appourchaux et al. 2012; Lund et al. 2017), resulting in a low S/N  $\langle A_\nu \rangle$  as seen in Figure 3. Note however that the measured oscillation frequencies of such stars are very precise because of the narrow linewidths, and the resulting

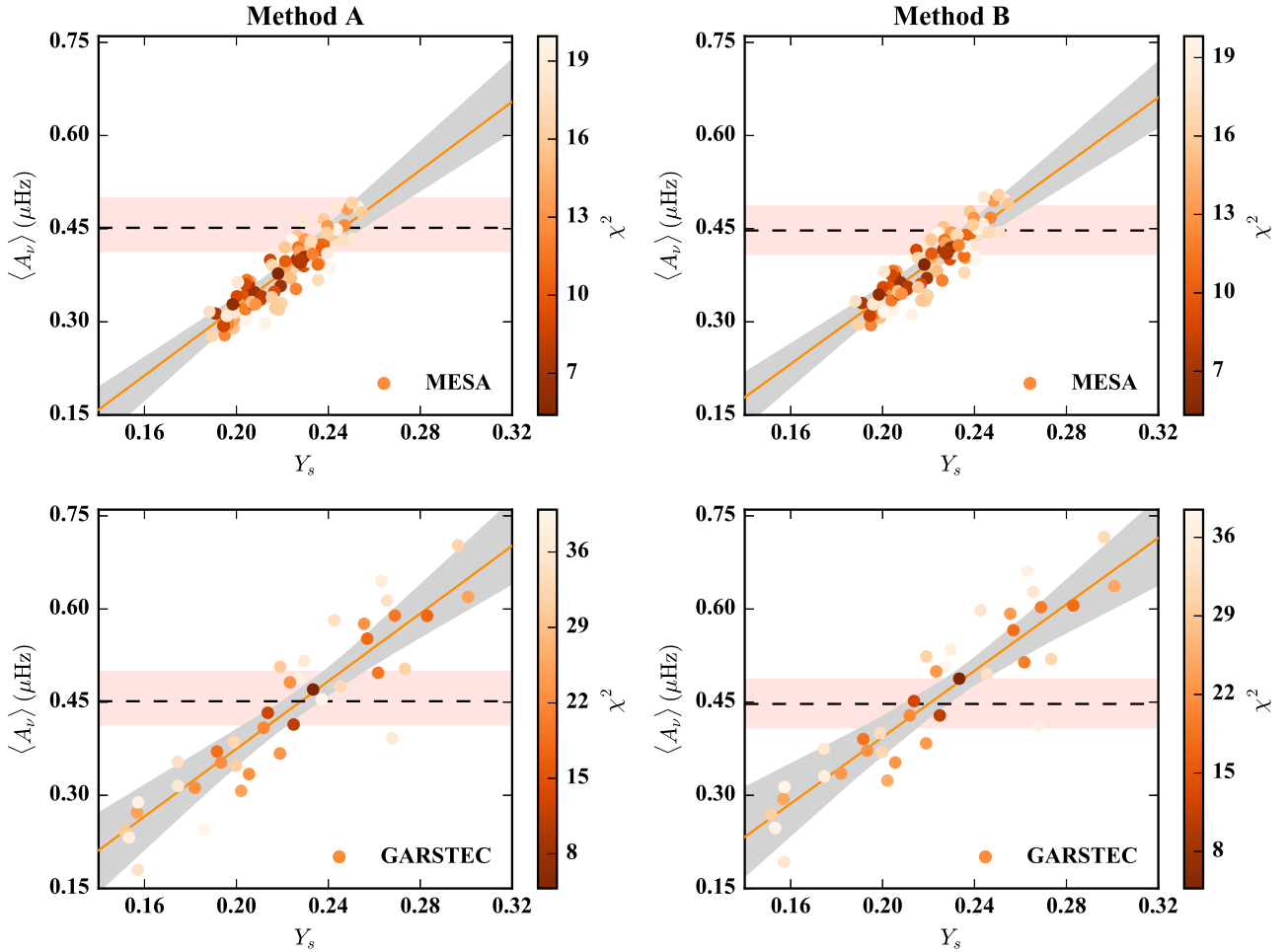


**Figure 2.** Calibration of the observed average amplitude against the surface helium abundance for 16 Cyg A. The two columns represent the results obtained using the two different fitting methods, while the two rows show the two different sets of the calibration models. The dashed line represents the observed average amplitude with  $1\sigma$  uncertainty shown by the shaded region around it. The points in a panel represent the average amplitude for the models with the colour indicating their  $\chi^2$  value (as defined in Eq. 9). The continuous line is a weighted straight-line fit to the points with the band around it representing the Monte-Carlo regression uncertainty.

frequency ratios have large S/N. On the other hand, the linewidths for the high-mass stars are very broad and the oscillation frequencies have large errorbars. Although this is not a problem for the  $\langle A_\nu \rangle$  because of the strong helium signature arising from such stars, the frequency ratios have poor S/N (see Figure 3).

Assuming that the tightness of the correlation in the calibration diagram depends on the S/N of the frequency ratios, the rejection of all the 28 stars can be understood from Figure 3. The low-mass stars are rejected primarily because of the poor S/N of  $\langle A_\nu \rangle$ , while the high-mass stars are rejected because of the poor S/N of the frequency ratios. It should be noted that the overshoot plays an important role together with the mass in determining the size of the convective core for the high-mass stars. Since we select the calibration models based on the frequency ratios, which puts constraint on the convective core size, there is a degeneracy between the mass and overshoot – the larger the overshoot, the smaller the mass. This trade-off between the mass and overshoot results calibration models with significantly differ-

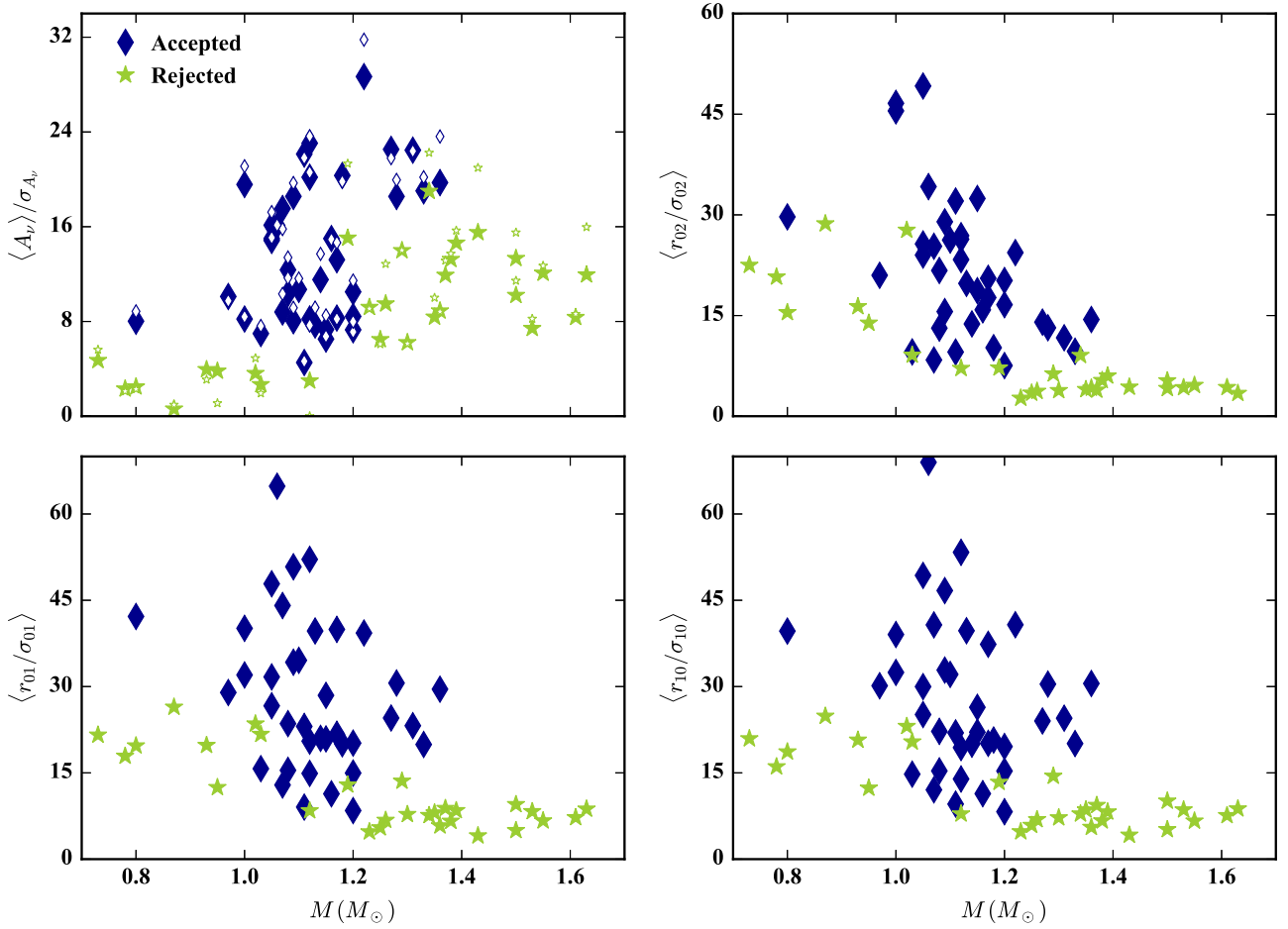
ent masses, adding more scatter in the calibration diagram for the high-mass stars.

## 4.2 Surface helium abundance

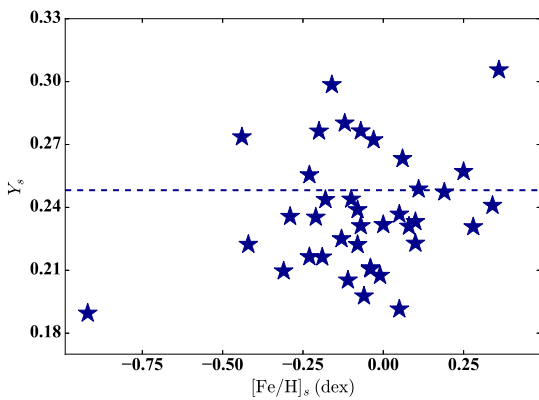
The surface helium abundance for all the 38 stars obtained using the different fitting methods and different sets of calibration models are listed in Table 3. The centre of the range spanned by the four estimates of  $Y_s$  is shown in Figure 4 as a function of the surface metallicity. Note in the figure that a large fraction of the stars have  $Y_s$  below the standard Big Bang nucleosynthesis value ( $0.2482 \pm 0.0007$ ; Steigman 2010), confirming the significant settling of the helium in these stars as is known to happen in the Sun. The table also lists the settling of the helium,  $\delta Y = Y_i - Y_s$ , and heavy elements,  $\delta Z = Z_i - Z_s$ , predicted by the best-fitting MESA models. This will be used in Section 4.4 to get the preliminary estimates of the initial abundances.

Figure 5 shows comparisons among the different estimates of  $Y_s$ . As we can see from the bottom panels, the val-





**Figure 3.** Signal-to-noise ratio for the various observables as a function of the mass (mass is taken from Verma et al. 2017). The top left panel shows the S/N of the average amplitude for all the stars in the LEGACY sample. The big-filled and small-open symbols in that panel are obtained using the fitting Methods A and B, respectively. The rest of the panels show the S/N of the three ratios averaged over the radial order. The diamond points represent the 38 stars for which both the requirements are met (see the text), while the star symbols represent those for which at least one requirement is not fulfilled.



**Figure 4.** Surface helium abundance as a function of the surface metallicity for all the 38 stars. The points represent the centre of the helium range spanned by the four estimates listed in Table 3. The horizontal dashed line represents the primordial helium abundance.

ues obtained using the two different fitting methods agree well within  $1\sigma$ . For this reason and for the sake of clarity, we shall present the results only from the Method A in the subsequent sections. The envelope helium abundances obtained using the different sets of calibration models also agree within  $1\sigma$  for most of the stars as seen in the top panels of Figure 5, except for a few high-mass stars. There is, however, a noticeable systematic shift of approximately 0.02, with the MESA models giving systematically larger values of  $Y_s$  than the GARSTEC models. This offset is due to the differences in the input physics used in the two sets of models. We shall show in Section 4.3 using the YREC models that this small systematic difference is a result of the fact that the MESA includes atomic diffusion and the GARSTEC does not.

We have 3 solar-type stars with previously determined  $Y_s$ : the Sun, 16 Cyg A and 16 Cyg B. The solar helium abundance was determined using the intermediate degree oscillation frequencies ( $0.248 \pm 0.003$ ; Basu 1998). The  $Y_s$  for the binary system 16 Cyg A & B was estimated using

**Table 3.** Envelope helium abundance of all the 38 stars obtained using the two different fitting methods (A and B) and two sets of calibration models (MESA and GARSTEC). The last two columns are the settling of the helium and heavy elements obtained using the best-fitting MESA models.

KIC	Method A		Method B		$\delta Y = Y_i - Y_s$	$\delta Z = Z_i - Z_s$
	MESA	GARSTEC	MESA	GARSTEC		
3427720	0.205 <sup>+0.015</sup> <sub>-0.014</sub>	0.193 <sup>+0.016</sup> <sub>-0.015</sub>	0.201 <sup>+0.014</sup> <sub>-0.012</sub>	0.191 <sup>+0.015</sup> <sub>-0.013</sub>	0.0262	0.0016
3632418	0.304 <sup>+0.016</sup> <sub>-0.018</sub>	0.248 <sup>+0.009</sup> <sub>-0.010</sub>	0.313 <sup>+0.017</sup> <sub>-0.019</sub>	0.249 <sup>+0.010</sup> <sub>-0.010</sub>	0.0717	0.0041
3656476	0.271 <sup>+0.024</sup> <sub>-0.018</sub>	0.267 <sup>+0.029</sup> <sub>-0.022</sub>	0.250 <sup>+0.019</sup> <sub>-0.014</sub>	0.243 <sup>+0.024</sup> <sub>-0.017</sub>	0.0368	0.0043
3735871	0.217 <sup>+0.016</sup> <sub>-0.014</sub>	0.206 <sup>+0.019</sup> <sub>-0.016</sub>	0.215 <sup>+0.017</sup> <sub>-0.014</sub>	0.204 <sup>+0.020</sup> <sub>-0.017</sub>	0.0136	0.0009
4914923	0.242 <sup>+0.012</sup> <sub>-0.013</sub>	0.222 <sup>+0.008</sup> <sub>-0.009</sub>	0.240 <sup>+0.014</sup> <sub>-0.015</sub>	0.220 <sup>+0.009</sup> <sub>-0.010</sub>	0.0411	0.0033
5184732	0.291 <sup>+0.028</sup> <sub>-0.026</sub>	0.313 <sup>+0.033</sup> <sub>-0.031</sub>	0.293 <sup>+0.027</sup> <sub>-0.028</sub>	0.320 <sup>+0.033</sup> <sub>-0.034</sub>	0.0345	0.0043
6106415	0.222 <sup>+0.014</sup> <sub>-0.012</sub>	0.203 <sup>+0.011</sup> <sub>-0.009</sub>	0.218 <sup>+0.014</sup> <sub>-0.013</sub>	0.201 <sup>+0.011</sup> <sub>-0.010</sub>	0.0401	0.0028
6116048	0.227 <sup>+0.011</sup> <sub>-0.011</sub>	0.206 <sup>+0.008</sup> <sub>-0.008</sub>	0.228 <sup>+0.010</sup> <sub>-0.011</sub>	0.205 <sup>+0.008</sup> <sub>-0.008</sub>	0.0560	0.0029
6225718	0.235 <sup>+0.009</sup> <sub>-0.009</sub>	0.227 <sup>+0.009</sup> <sub>-0.009</sub>	0.235 <sup>+0.009</sup> <sub>-0.010</sub>	0.229 <sup>+0.009</sup> <sub>-0.010</sub>	0.0413	0.0027
6603624	0.241 <sup>+0.018</sup> <sub>-0.017</sub>	0.221 <sup>+0.008</sup> <sub>-0.007</sub>	0.238 <sup>+0.021</sup> <sub>-0.018</sub>	0.221 <sup>+0.008</sup> <sub>-0.007</sub>	0.0388	0.0046
6933899	0.223 <sup>+0.009</sup> <sub>-0.010</sub>	0.194 <sup>+0.008</sup> <sub>-0.008</sub>	0.218 <sup>+0.009</sup> <sub>-0.009</sub>	0.193 <sup>+0.008</sup> <sub>-0.008</sub>	0.0346	0.0025
7296438	0.247 <sup>+0.025</sup> <sub>-0.023</sub>	0.233 <sup>+0.019</sup> <sub>-0.018</sub>	0.262 <sup>+0.030</sup> <sub>-0.021</sub>	0.245 <sup>+0.024</sup> <sub>-0.017</sub>	0.0434	0.0039
7510397	0.261 <sup>+0.018</sup> <sub>-0.018</sub>	0.209 <sup>+0.008</sup> <sub>-0.007</sub>	0.251 <sup>+0.017</sup> <sub>-0.016</sub>	0.210 <sup>+0.009</sup> <sub>-0.008</sub>	0.0727	0.0042
7680114	0.198 <sup>+0.018</sup> <sub>-0.011</sub>	0.186 <sup>+0.018</sup> <sub>-0.011</sub>	0.197 <sup>+0.014</sup> <sub>-0.009</sub>	0.185 <sup>+0.016</sup> <sub>-0.010</sub>	0.0437	0.0040
7940546	0.331 <sup>+0.025</sup> <sub>-0.028</sub>	0.222 <sup>+0.012</sup> <sub>-0.013</sub>	0.328 <sup>+0.023</sup> <sub>-0.025</sub>	0.229 <sup>+0.013</sup> <sub>-0.014</sub>	0.0809	0.0048
8006161	0.246 <sup>+0.025</sup> <sub>-0.020</sub>	0.258 <sup>+0.029</sup> <sub>-0.023</sub>	0.224 <sup>+0.019</sup> <sub>-0.019</sub>	0.231 <sup>+0.022</sup> <sub>-0.022</sub>	0.0208	0.0023
8179536	0.270 <sup>+0.038</sup> <sub>-0.033</sub>	0.280 <sup>+0.040</sup> <sub>-0.035</sub>	0.264 <sup>+0.040</sup> <sub>-0.034</sub>	0.270 <sup>+0.041</sup> <sub>-0.035</sub>	0.0594	0.0043
8228742	0.230 <sup>+0.020</sup> <sub>-0.019</sub>	0.207 <sup>+0.011</sup> <sub>-0.010</sub>	0.237 <sup>+0.018</sup> <sub>-0.018</sub>	0.211 <sup>+0.010</sup> <sub>-0.010</sub>	0.0617	0.0035
8379927	0.250 <sup>+0.008</sup> <sub>-0.008</sub>	0.237 <sup>+0.008</sup> <sub>-0.008</sub>	0.251 <sup>+0.009</sup> <sub>-0.008</sub>	0.237 <sup>+0.008</sup> <sub>-0.008</sub>	0.0254	0.0014
8394589	0.253 <sup>+0.025</sup> <sub>-0.022</sub>	0.215 <sup>+0.018</sup> <sub>-0.016</sub>	0.257 <sup>+0.021</sup> <sub>-0.023</sub>	0.219 <sup>+0.016</sup> <sub>-0.017</sub>	0.0561	0.0024
8694723	0.251 <sup>+0.016</sup> <sub>-0.017</sub>	0.194 <sup>+0.014</sup> <sub>-0.015</sub>	0.250 <sup>+0.016</sup> <sub>-0.015</sub>	0.197 <sup>+0.014</sup> <sub>-0.013</sub>	0.0860	0.0028
8760414	0.203 <sup>+0.022</sup> <sub>-0.019</sub>	0.178 <sup>+0.011</sup> <sub>-0.009</sub>	0.201 <sup>+0.018</sup> <sub>-0.018</sub>	0.176 <sup>+0.009</sup> <sub>-0.009</sub>	0.0695	0.0012
8938364	0.234 <sup>+0.010</sup> <sub>-0.010</sub>	0.220 <sup>+0.010</sup> <sub>-0.009</sub>	0.227 <sup>+0.010</sup> <sub>-0.010</sub>	0.216 <sup>+0.010</sup> <sub>-0.009</sub>	0.0603	0.0031
9098294	0.256 <sup>+0.015</sup> <sub>-0.016</sub>	0.247 <sup>+0.016</sup> <sub>-0.016</sub>	0.243 <sup>+0.017</sup> <sub>-0.014</sub>	0.231 <sup>+0.018</sup> <sub>-0.014</sub>	0.0457	0.0026
9139151	0.233 <sup>+0.014</sup> <sub>-0.014</sub>	0.216 <sup>+0.015</sup> <sub>-0.015</sub>	0.230 <sup>+0.014</sup> <sub>-0.012</sub>	0.213 <sup>+0.014</sup> <sub>-0.013</sub>	0.0196	0.0013
9410862	0.221 <sup>+0.021</sup> <sub>-0.021</sub>	0.206 <sup>+0.018</sup> <sub>-0.018</sub>	0.211 <sup>+0.016</sup> <sub>-0.021</sub>	0.198 <sup>+0.014</sup> <sub>-0.019</sub>	0.0528	0.0022
9965715	0.312 <sup>+0.061</sup> <sub>-0.053</sub>	0.253 <sup>+0.032</sup> <sub>-0.027</sub>	0.273 <sup>+0.050</sup> <sub>-0.046</sub>	0.235 <sup>+0.026</sup> <sub>-0.023</sub>	0.0871	0.0041
10068307	0.257 <sup>+0.013</sup> <sub>-0.015</sub>	0.251 <sup>+0.010</sup> <sub>-0.011</sub>	0.262 <sup>+0.013</sup> <sub>-0.011</sub>	0.249 <sup>+0.010</sup> <sub>-0.009</sub>	0.0675	0.0029
10079226	0.257 <sup>+0.032</sup> <sub>-0.031</sub>	0.244 <sup>+0.032</sup> <sub>-0.030</sub>	0.252 <sup>+0.034</sup> <sub>-0.027</sub>	0.240 <sup>+0.035</sup> <sub>-0.027</sub>	0.0262	0.0017
10162436	0.324 <sup>+0.021</sup> <sub>-0.022</sub>	0.273 <sup>+0.016</sup> <sub>-0.016</sub>	0.324 <sup>+0.022</sup> <sub>-0.022</sub>	0.273 <sup>+0.016</sup> <sub>-0.016</sub>	0.0708	0.0039
10454113	0.279 <sup>+0.017</sup> <sub>-0.015</sub>	0.276 <sup>+0.018</sup> <sub>-0.016</sub>	0.278 <sup>+0.018</sup> <sub>-0.015</sub>	0.273 <sup>+0.019</sup> <sub>-0.016</sub>	0.0483	0.0029
10516096	0.212 <sup>+0.012</sup> <sub>-0.012</sub>	0.204 <sup>+0.011</sup> <sub>-0.011</sub>	0.204 <sup>+0.010</sup> <sub>-0.010</sub>	0.198 <sup>+0.010</sup> <sub>-0.010</sub>	0.0555	0.0033
10644253	0.270 <sup>+0.026</sup> <sub>-0.020</sub>	0.256 <sup>+0.026</sup> <sub>-0.020</sub>	0.270 <sup>+0.030</sup> <sub>-0.022</sub>	0.257 <sup>+0.029</sup> <sub>-0.021</sub>	0.0145	0.0010
10963065	0.233 <sup>+0.022</sup> <sub>-0.020</sub>	0.210 <sup>+0.019</sup> <sub>-0.019</sub>	0.221 <sup>+0.020</sup> <sub>-0.016</sub>	0.199 <sup>+0.017</sup> <sub>-0.013</sub>	0.0525	0.0030
12009504	0.256 <sup>+0.029</sup> <sub>-0.029</sub>	0.227 <sup>+0.019</sup> <sub>-0.018</sub>	0.239 <sup>+0.023</sup> <sub>-0.024</sub>	0.222 <sup>+0.016</sup> <sub>-0.016</sub>	0.0713	0.0045
12069424	0.246 <sup>+0.017</sup> <sub>-0.014</sub>	0.228 <sup>+0.017</sup> <sub>-0.014</sub>	0.240 <sup>+0.015</sup> <sub>-0.014</sub>	0.220 <sup>+0.015</sup> <sub>-0.014</sub>	0.0404	0.0033
12069449	0.255 <sup>+0.010</sup> <sub>-0.010</sub>	0.225 <sup>+0.008</sup> <sub>-0.008</sub>	0.248 <sup>+0.009</sup> <sub>-0.009</sub>	0.219 <sup>+0.007</sup> <sub>-0.007</sub>	0.0371	0.0032
12258514	0.250 <sup>+0.007</sup> <sub>-0.008</sub>	0.215 <sup>+0.007</sup> <sub>-0.008</sub>	0.250 <sup>+0.007</sup> <sub>-0.007</sub>	0.213 <sup>+0.007</sup> <sub>-0.007</sub>	0.0471	0.0034

the helium glitch signature in the low degree oscillation frequencies in the way it is determined in the current work (minor differences lie in the details of the methods and in the length of the time series used to compute the observed oscillation frequencies). [Verma et al. \(2014a\)](#) found the  $Y_s$  for 16 Cyg A to be in the range 0.231–0.251 and for 16 Cyg B in the range 0.218–0.266. We can see from Table 3 that the different estimates of  $Y_s$  for 16 Cyg A (KIC 12069424) & B (KIC 12069449) are in good agreement, including the previous determinations.

We used Sun-as-a-star data from [Lund et al. \(2017\)](#) to determine the solar helium abundance using the Method A. We found  $Y_s$  to be  $0.240^{+0.025}_{-0.015}$  and  $0.223^{+0.022}_{-0.013}$  for the MESA and GARSTEC calibration models, respectively. Note that the estimate obtained using the MESA is again larger than the one obtained using the GARSTEC by roughly the same amount (0.02). Since the  $Y_s$  obtained using the MESA models is closer to the helioseismic value, we may expect the values derived using the MESA models for the other stars with masses and metallicities similar to the Sun to be more accu-

rate than the values obtained using the GARSTEC models. This is also supported by the fact that the diffusion models are more realistic than the non-diffusion ones for such stars.

Element settling in relatively massive stars (mass can be lower than  $1.2 M_\odot$  for a metallicity of  $-0.5$  dex) is not very well understood. Models of atomic diffusion predict excessive settling of the helium and heavy elements in the envelope of such stars ([Morel & Thévenin 2002](#)). This does not mean that the models of atomic diffusion are wrong, rather it points towards the importance of the non-standard processes that compete with atomic diffusion (see e.g. [Turcotte et al. 1998](#), also see Section 4.4 for further discussion and references). For such stars, the non-diffusion models are expected to be closer to the real stars in terms of reproducing the observed surface abundances (unless the non-standard processes are better understood, and are included in the stellar model calculations along with atomic diffusion), hence the  $Y_s$  obtained using the non-diffusion GARSTEC models are expected to be more accurate. The range of  $Y_s$  obtained using the MESA and GARSTEC models provides the largest pos-

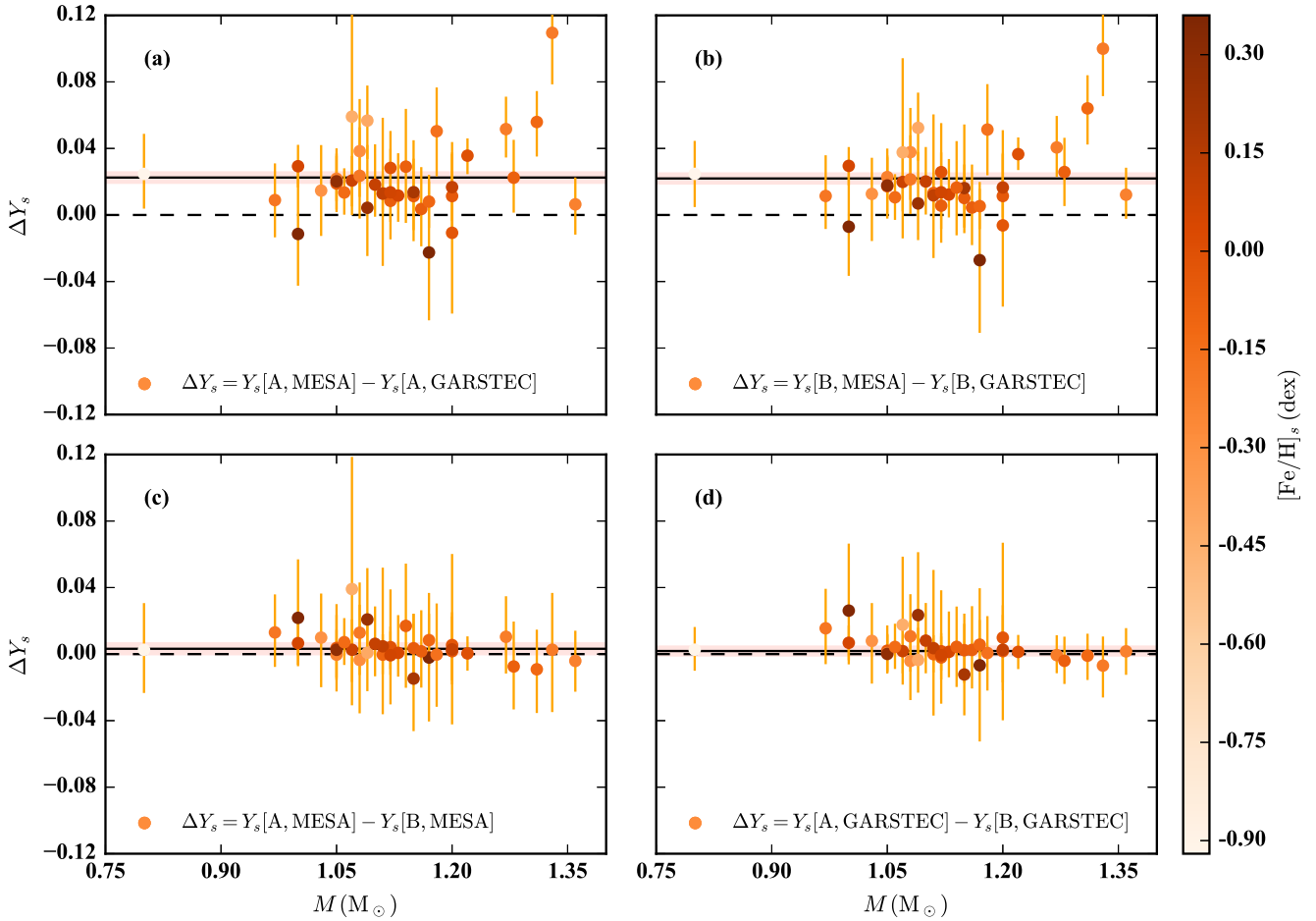


**Figure 5.** Comparison of the different estimates of the envelope helium abundance for all the 38 stars. The panels (a–b) compare the estimates obtained using the different sets of calibration models (MESA and GARSTEC) for a given fitting method, while the panels (c–d) compare the estimates obtained using the different fitting methods (A and B) for a given set of calibration models. The horizontal dashed line indicates the zero level. The continuous line is the weighted average of the points with the band around it representing the  $1\sigma$  uncertainty. The colour represents the metallicity of the stars.

sible systematic uncertainty expected from the uncertainties in the chemical element transport in the envelope, as these two sets of models represent the two extreme cases of the helium settling.

### 4.3 Impact of the atomic diffusion

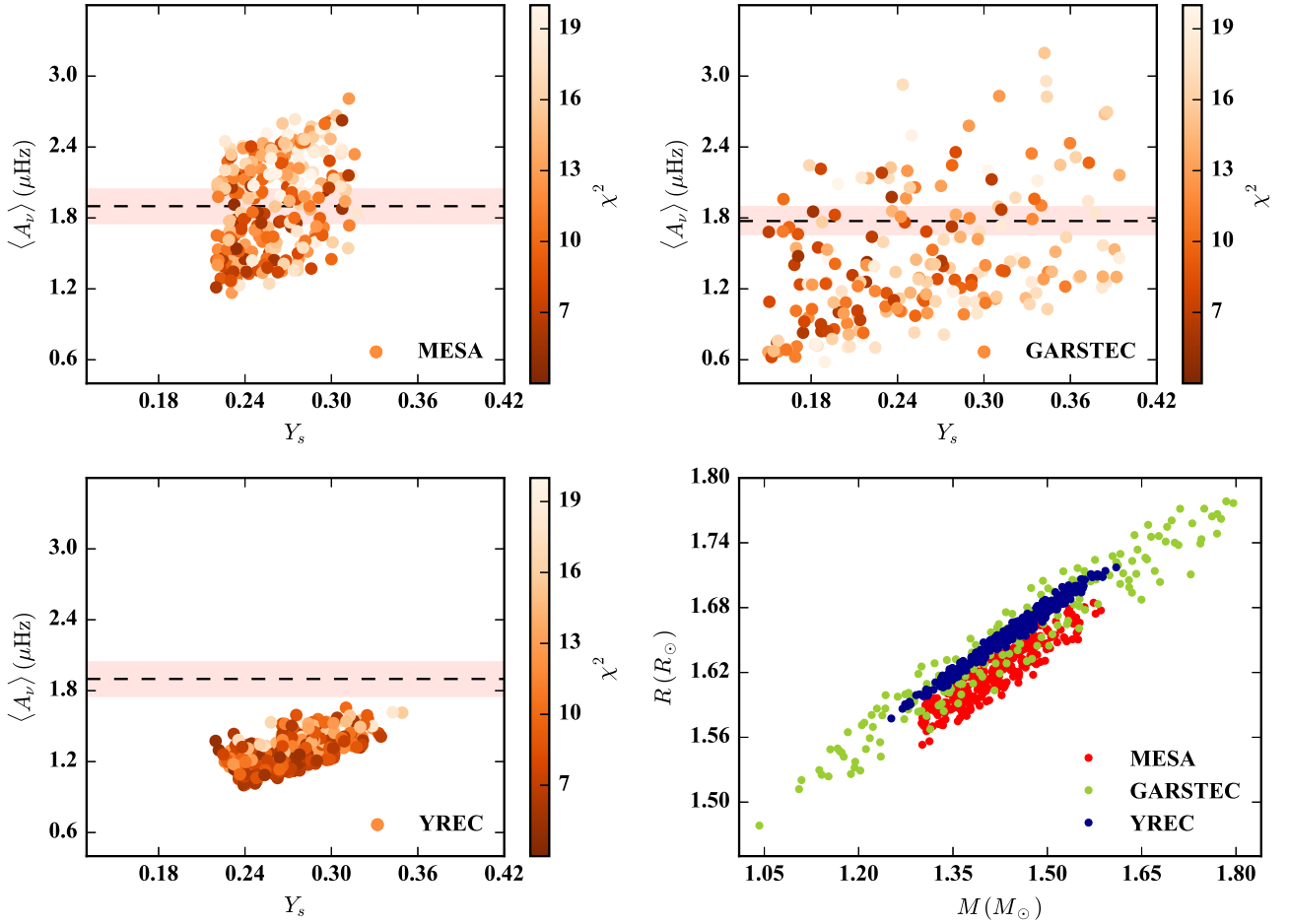
To demonstrate the source of the systematic shift of about 0.02 seen in the top panels of Figure 5, we constructed two sets of YREC models differing only in the diffusion (one includes atomic diffusion and other does not). We used the fitting Method A for both the sets of models to determine  $Y_s$  for 16 Cyg A & B, KIC 6106415 and 6116048. We can see in Table 4 that these estimates of  $Y_s$  agree well with those presented in Table 3, pointing towards the robustness of  $Y_s$  determination. We can also see that the envelope helium abundance obtained using the diffusion models are systematically larger than those found with the non-diffusion models by about 0.02, confirming the fact that the systematic shift is indeed a result of the uncertainties in the chemical

element transport in the stellar interior. Table 4 also lists the settling predicted by the best-fitting YREC (diffusion) models, and can be compared with those obtained with the MESA (see Table 3). A good level of agreement reassures the robustness of  $\delta Y$  and  $\delta Z$  determinations against the uncertainties in the stellar properties and the input physics. This however does not necessarily mean that the estimates are accurate, because the largest uncertainty on  $\delta Y$  and  $\delta Z$  results from the neglect of the various physical processes that compete with the atomic diffusion, which have been ignored in both the sets of models.

We wish to take here an example of YREC models to point out one caveat related to the determination of  $Y_s$  through the model calibration. Every choice of the vector  $(M, Y_i, [\text{Fe}/\text{H}]_i, \alpha_{\text{MLT}}, \alpha_{\text{OV}})$  for different values of  $M, Y_i, [\text{Fe}/\text{H}]_i, \alpha_{\text{MLT}}$  and  $\alpha_{\text{OV}}$  results a point in the calibration diagram. This means that, in principle, it is possible to choose a set of these vectors such that the calibration diagram has tight artificial correlation irrespective of the observed data quality (essentially disregarding systematically some of the

**Table 4.** Envelope helium abundance of four stars obtained using the Method A and both sets of YREC models. The last two columns are the settling of the helium and heavy elements obtained using the best-fitting YREC (diffusion) models.

Star	YREC (dif.)	YREC (nodif.)	$\delta Y = Y_i - Y_s$	$\delta Z = Z_i - Z_s$
16 Cyg A	$0.245^{+0.024}_{-0.019}$	$0.232^{+0.017}_{-0.014}$	0.0373	0.0038
16 Cyg B	$0.274^{+0.016}_{-0.016}$	$0.245^{+0.009}_{-0.009}$	0.0389	0.0034
KIC 6106415	$0.223^{+0.013}_{-0.012}$	$0.211^{+0.014}_{-0.012}$	0.0389	0.0029
KIC 6116048	$0.223^{+0.011}_{-0.011}$	$0.210^{+0.012}_{-0.012}$	0.0545	0.0027

**Figure 6.** Calibration diagrams (the top panels and the bottom left panel) for KIC 2837475 obtained using the Method A (see the caption for Figure 2). The corresponding models are also shown in a mass-radius diagram in the bottom right panel.

vectors that lead to off-the-trend points in the calibration diagram). This may also happen in practice, which is illustrated below for KIC 2837475. KIC 2837475 is one of the 28 rejected stars with the poor S/N frequency ratios ( $\langle r_{02}/\sigma_{02} \rangle = 4.1$ ,  $\langle r_{01}/\sigma_{01} \rangle = 5.0$  and  $\langle r_{10}/\sigma_{10} \rangle = 5.2$ ).

Figure 6 shows the calibration diagrams for KIC 2837475. Note that this star has relatively high-mass ( $\approx 1.5 M_\odot$ ), and hence the corresponding models in the figure exclude the atomic diffusion in all the three sets. We can see in the figure that, despite the poor S/N of the frequency ratios, the YREC models show reasonably tight correlation in the calibration diagram. On the other hand, the MESA and GARSTEC models show much larger scatter. This is partly

due to the fact that the YREC models by construction have  $T_{\text{eff}}$  and  $[\text{Fe}/\text{H}]_s$  within  $1\sigma$  of the observations. More importantly, however, this is a result of using the semi-empirical scaling relations (Kjeldsen & Bedding 1995) to constrain the initial parameter space. We can see in the mass-radius diagram that the YREC models are just a subset of the MESA and GARSTEC models, showing much tighter relation between the mass and radius.

For the stars with the mass and metallicity similar to the Sun, like the ones listed in Table 4, the scaling relations are known to work well, and hence resulting in consistent values for the  $Y_s$ . However, for the relatively high-mass stars, like the one shown in Figure 6, the artificial corre-

lation can provide highly biased estimate of  $Y_s$ . To reduce the possibility of introducing misleading tight correlations in the calibration diagrams, we considered all the relevant parameters free including the mixing-length and the overshoot for both the MESA and GARSTEC. Furthermore, we sampled the initial parameter space uniformly, and selected the calibration models solely based on the observations.

#### 4.4 Galactic enrichment ratio

The determination of the enrichment ratio requires the initial values of the helium and metal mass fractions, which rely on the measurements of the corresponding surface values as well as on the models of the chemical element transport in the stellar envelope. The inclusion of the atomic diffusion in the solar models reduced significantly the discrepancies between the model and helioseismic data (see e.g., Christensen-Dalsgaard et al. 1993; Guenther et al. 1996), pointing towards the importance of this process in the solar interior. However, the same models of the atomic diffusion predict complete depletion of the helium and heavy elements in the envelope of the stars of masses approximately greater than  $1.4 M_\odot$  (also depends on the metallicity and age). This is unrealistic given the measurements of the heavy element abundances in the A and F-type stars (see e.g. Varenne & Monier 1999) and the detections of the helium glitch signature in the F-type stars (see Verma et al. 2017). Additional processes like radiative levitation, mass loss, turbulence etc. can potentially reduce the settling (see e.g. Vauclair et al. 1978a,b; Vauclair 1999; Richer et al. 2000), and lead to a better agreement between the observed and model predicted surface abundances (see e.g. Richer et al. 2000; Théado & Vauclair 2001; Michaud et al. 2011; Castro et al. 2016). A detailed investigation of the settling including the microscopic diffusion, radiative levitation and other processes is beyond the scope of this work.

The point of the above discussion is that the excessive settling of the helium and heavy elements predicted by the standard stellar models with atomic diffusion (excluding the non-standard processes) for the relatively massive and metal poor stars is unrealistic. Hence the estimated  $\delta Y$  and  $\delta Z$  as well as  $Y_i$  and  $Z_i$  are inaccurate for such stars. For this reason, to determine the enrichment ratio we shall consider only those stars for which the stellar models predict helium settling below a threshold (the mass alone is not a good quantity for this purpose because the settling also depends substantially on the metallicity and evolutionary state).

We estimated the initial abundances from the measured surface values using the settling from the best-fitting MESA models. Figure 7 shows  $Y_i$  against  $Z_i$  with the different thresholds on the helium settling. We fitted a straight line to  $Y_i$  as a function of  $Z_i$  using the weighted least squares method to get the “preliminary” estimates of the primordial helium abundance (the intercept,  $Y_p$ ) and the galactic enrichment ratio (the slope,  $\Delta Y/\Delta Z$ ). Note that only the uncertainty on  $Y_i$  is currently used as weight in producing the linear relationship. The reason is that there are only a few data points at high  $Z_i$  with rather large errorbars, and hence including the uncertainty on  $Z_i$  in the fit makes the slope and intercept highly uncertain. Moreover, the inclusion of this uncertainty makes the optimization process nonlinear, and fits suffer from convergence issues due to poor

constraint on the slope and intercept. We made two unsuccessful attempts to fit the data with uncertainties in both  $Y_i$  and  $Z_i$  using *bivariate correlated errors and intrinsic scatter* (BCES; Akritas & Bershady 1996; Nemmen et al. 2012)<sup>1</sup> and *affine invariant markov chain monte carlo ensemble sampler* (emcee: The MCMC Hammer; Goodman & Weare 2010; Foreman-Mackey et al. 2013)<sup>2</sup>. Clearly we need either more data points at high  $Z_i$  or more precise measurements of the surface metallicity to perform a proper fitting including the uncertainties in both  $Y_i$  and  $Z_i$ . In the foreseeable future, we do not expect much improvement in the precision of the metallicity measurements, however the sample size is anticipated to get much bigger in the *Planetary Transits and Oscillations of stars* (PLATO; Rauer et al. 2014) era. To simulate larger sample size, we duplicated the data points with  $Z_i > 0.025$  (the data points with the largest  $Z_i$  errorbars), and tried fitting the straight line with errors in both  $Y_i$  and  $Z_i$  using emcee. Although results are meaningless due to artificially added data points, we confirm that the emcee chains do converge now. Therefore larger sample size in the future can potentially alleviate the problem of poor precision of  $Z_i$ .

We note from the legends in Figure 7 the precision of  $Y_p$  and  $\Delta Y/\Delta Z$  as a function of the threshold on  $\delta Y$ . The precision initially increases until  $\delta Y = 0.045$  because of the increase in the number of the data points. However, as we further increase the threshold, the precision drops and the trend becomes meaningless eventually when including all the 38 stars. We attribute this behaviour to the unreliable estimates of  $Y_i$  and  $Z_i$  for the stars with  $\delta Y > 0.045$ . For this reason, we recommend the estimates of  $Y_p = 0.244 \pm 0.019$  and  $\Delta Y/\Delta Z = 1.226 \pm 0.849$  from the middle left panel with  $\delta Y < 0.045$ . To test the robustness of the results, we also fitted a straight line to  $Z_i$  as a function of  $Y_i$  using weighted least squares method (weight being the uncertainty on  $Z_i$ ), and inverted the relationship to get  $Y_p$  and  $\Delta Y/\Delta Z$ . For the panel corresponding to  $\delta Y < 0.045$ , we find  $Y_p = 0.094 \pm 0.128$  and  $\Delta Y/\Delta Z = 8.019 \pm 3.618$ . Clearly the uncertainties on the estimates are very large due to the large uncertainty on  $Z_i$ . We wish to further point out that the quoted uncertainty on  $Z_i$  represents only the statistical uncertainty. It may also have systematic uncertainties arising from the uncertainties in the models of stellar atmosphere (which affects the measurement of  $[\text{Fe}/\text{H}]_s$ ) and in the solar abundances (which affects the conversion between  $[\text{Fe}/\text{H}]_s$  and  $Z_s$ ). Note that once we have large enough sample, we can alleviate the problem of poor precision of  $Z_i$ , estimate the impact of the systematic uncertainty in  $Z_i$ , and also take more conservative approach and restrict the stars according to  $\delta Y < 0.040$  to gain more confidence in the estimates of  $Y_p$  and  $\Delta Y/\Delta Z$ .

The “simple” models of galactic chemical evolution predict a linear relationship between  $Y_i$  and  $Z_i$  (see e.g. Hacyan et al. 1976), however the reality may be more complex. Recent studies indicate towards a mildly quadratic relationship between  $Y_i$  and  $Z_i$  (West & Heger 2013). It is currently not possible to constrain a quadratic relationship given the small sample size and large errorbars, however

<sup>1</sup> <https://github.com/rsnemmen/BCES>

<sup>2</sup> <http://dfm.io/emcee/current/>



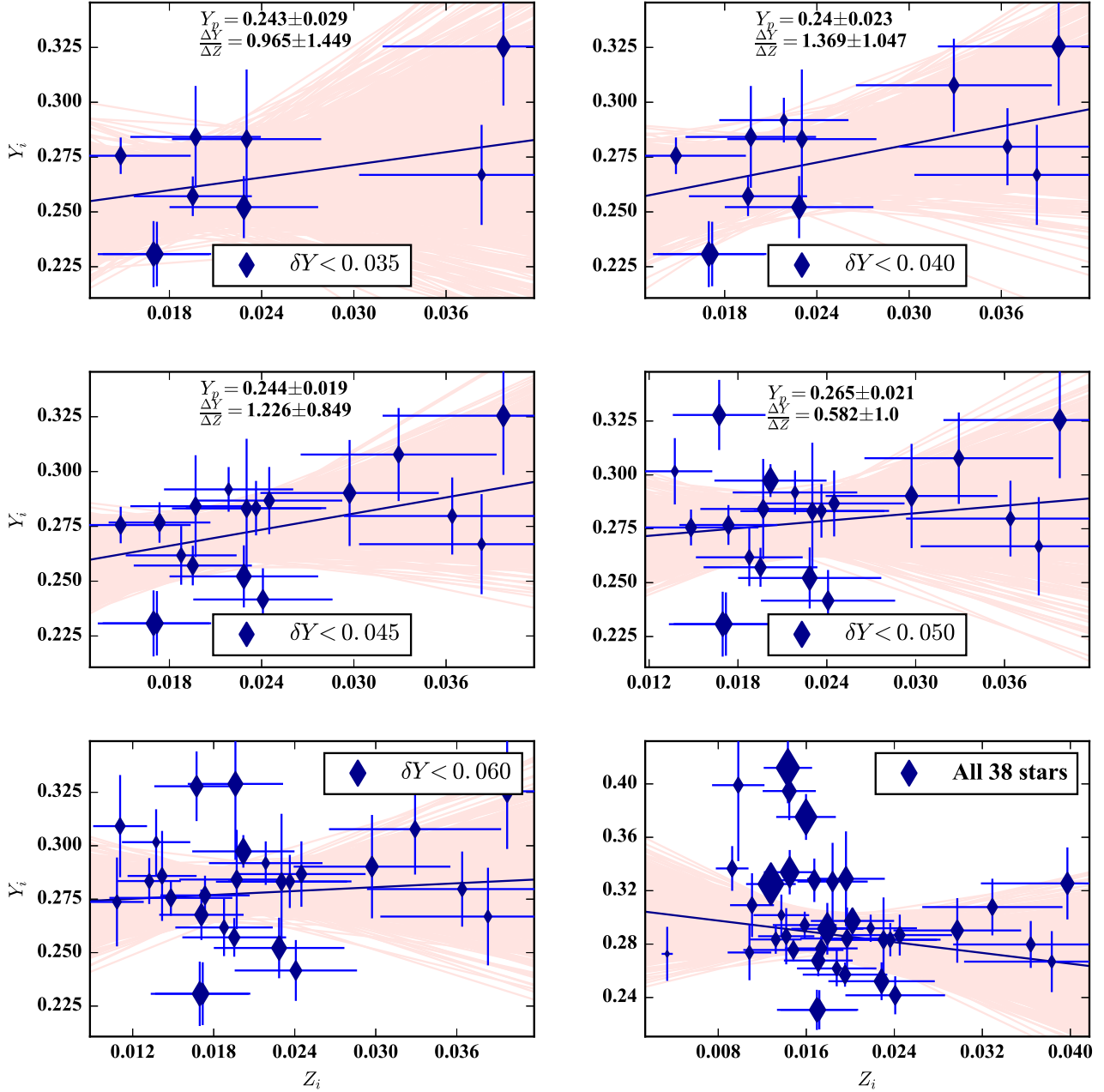


**Figure 7.** Initial helium mass fraction as a function of the initial metal mass fraction. Different panels show the stars with the helium settling below a threshold. The points are exponentially scaled with the mass. The blue line is a weighted straight-line fit to the points with the band around it representing the Monte-Carlo regression uncertainty. The intercept ( $Y_p$ ) and the slope ( $\Delta Y/\Delta Z$ ) of the fitted line is shown in the top four panels.

once the sample size grows bigger in the future, such studies would be very interesting.

## 5 SUMMARY

We used the helium glitch signature to estimate the surface helium abundance of the stars in the LEGACY sample. We found that  $Y_s$  for the low-mass stars can be determined reliably only if the number of the observed oscillation frequen-

cies and their precision are good enough to determine the average amplitude of the helium signature reliably. On the other hand, for the high-mass stars the larger uncertainties on the oscillation frequencies and hence the frequency ratios make  $Y_s$  determination difficult. We found 38 stars in the LEGACY sample for which  $Y_s$  can be determined reliably.

We extracted the glitch signatures from both, the oscillation frequencies and its second differences (Methods A and B), to quantify the systematic uncertainties on  $Y_s$  associated with the treatment of the background smooth component of

the oscillation frequency. The two methods provide  $Y_s$  within  $1\sigma$  for all the 38 stars.

We calibrated the observed average amplitude against the corresponding amplitude obtained from the model frequencies with different  $Y_s$  to estimate the surface helium abundance. Since the calibration involved the stellar models which are known to be uncertain, we used four different sets of models – one each using the MESA and GARSTEC and two using the YREC – with different input physics to quantify the uncertainties on  $Y_s$  associated with the uncertainties in the stellar physics. The different estimates of  $Y_s$  obtained in this manner agree within  $1\sigma$  for most of the stars. However, a systematic difference of about 0.02 was noted in  $Y_s$  when obtained using the diffusion and non-diffusion models.

We used the measurements of the surface abundances together with the settling predicted by the stellar models to compute the initial abundances. The initial abundances were used to derive the primordial helium abundance,  $Y_p = 0.244 \pm 0.019$ , and the enrichment ratio,  $\Delta Y/\Delta Z = 1.226 \pm 0.849$ . Currently in the *Kepler* era, the uncertainties are large because of the small sample size, and we hope to be able to determine these quantities with much higher precision in the PLATO era.

## ACKNOWLEDGEMENTS

Funding for the Stellar Astrophysics Centre is provided by The Danish National Research Foundation (Grant agreement no.: DNRFF106). We thank the anonymous referee for the constructive feedbacks. We are grateful to H. M. Antia for the discussions we had in the beginning of the project and for his comments on an earlier version of the manuscript. KR, AM and PR acknowledge support from the NIUS program of HBCSE (TIFR). SB is partially supported by NSF grant AST-1514676 and NASA grant NNX16AI09G. VSA acknowledges support from VILLUM FONDEN (Research Grant 10118). MNL acknowledges the support of The Danish Council for Independent Research | Natural Science (Grant DFF-4181-00415).

## REFERENCES

- Adelberger E. G., et al., 1998, *Reviews of Modern Physics*, **70**, 1265
- Aerts C., Christensen-Dalsgaard J., Kurtz D. W., 2010, *Asteroseismology*. Springer-Verlag, Heidelberg
- Akritis M. G., Bershady M. A., 1996, *ApJ*, **470**, 706
- Angulo C., et al., 1999, *Nuclear Physics A*, **656**, 3
- Antia H. M., Basu S., 1994, *A&AS*, **107**
- Appourchaux T., et al., 2012, *A&A*, **543**, A54
- Badnell N. R., Bautista M. A., Butler K., Delahaye F., Mendoza C., Palmeri P., Zeppen C. J., Seaton M. J., 2005, *MNRAS*, **360**, 458
- Baglin A., Auvergne M., Barge P., Deleuil M., Michel E., CoRoT Exoplanet Science Team 2009, in Pont F., Sasselov D., Holman M. J., eds, IAU Symposium Vol. 253, IAU Symposium. pp 71–81, doi:10.1017/S1743921308026252
- Ball W. H., Gizon L., 2014, *A&A*, **568**, A123
- Balser D. S., 2006, *AJ*, **132**, 2326
- Basu S., 1998, *MNRAS*, **298**, 719
- Basu S., Antia H. M., Narasimha D., 1994, *MNRAS*, **267**, 209
- Basu S., Mazumdar A., Antia H. M., Demarque P., 2004, *MNRAS*, **350**, 277
- Basu S., Chaplin W. J., Elsworth Y., 2010, *ApJ*, **710**, 1596
- Bellinger E. P., Angelou G. C., Hekker S., Basu S., Ball W., Guggenberger E., 2016, preprint, (arXiv:1607.02137)
- Borucki W., et al., 2009, in Pont F., Sasselov D., Holman M. J., eds, IAU Symposium Vol. 253, IAU Symposium. pp 289–299, doi:10.1017/S1743921308026513
- Broomhall A.-M., et al., 2014, *MNRAS*, **440**, 1828
- Buldgen G., Reese D. R., Dupret M. A., 2015, *A&A*, **583**, A62
- Buldgen G., Reese D. R., Dupret M. A., 2016a, *A&A*, **585**, A109
- Buldgen G., Salmon S. J. A. J., Reese D. R., Dupret M. A., 2016b, *A&A*, **596**, A73
- Casagrande L., Flynn C., Portinari L., Girardi L., Jimenez R., 2007, *MNRAS*, **382**, 1516
- Castro M., Duarte T., Pace G., do Nascimento J.-D., 2016, *A&A*, **590**, A94
- Chandrasekhar S., 1964, *ApJ*, **139**, 664
- Choi J., Dotter A., Conroy C., Cantiello M., Paxton B., Johnson B. D., 2016, *ApJ*, **823**, 102
- Christensen-Dalsgaard J., 1988, in Christensen-Dalsgaard J., Frandsen S., eds, IAU Symposium Vol. 123, Advances in Helio- and Asteroseismology. p. 295
- Christensen-Dalsgaard J., 2002, *Reviews of Modern Physics*, **74**, 1073
- Christensen-Dalsgaard J., 2008, *Ap&SS*, **316**, 113
- Christensen-Dalsgaard J., Dappen W., Lebreton Y., 1988, *Nature*, **336**, 634
- Christensen-Dalsgaard J., Proffitt C. R., Thompson M. J., 1993, *ApJ*, **403**, L75
- Claret A., Torres G., 2016, *A&A*, **592**, A15
- Corsaro E., De Ridder J., García R. A., 2015, *A&A*, **578**, A76
- Deheuvels S., et al., 2010, *A&A*, **514**, A31
- Demarque P., Woo J.-H., Kim Y.-C., Yi S. K., 2004, *ApJS*, **155**, 667
- Demarque P., Guenther D. B., Li L. H., Mazumdar A., Straka C. W., 2008, *Ap&SS*, **316**, 31
- Dotter A., Chaboyer B., Jevremović D., Kostov V., Baron E., Ferguson J. W., 2008, *ApJS*, **178**, 89
- Ferguson J. W., Alexander D. R., Allard F., Barman T., Bodnarik J. G., Hauschildt P. H., Heffner-Wong A., Tamanai A., 2005, *ApJ*, **623**, 585
- Foreman-Mackey D., Hogg D. W., Lang D., Goodman J., 2013, *PASP*, **125**, 306
- Formicola A., et al., 2004, *Physics Letters B*, **591**, 61
- Freytag B., Ludwig H.-G., Steffen M., 1996, *A&A*, **313**, 497
- Gai N., Basu S., Chaplin W. J., Elsworth Y., 2011, *ApJ*, **730**, 63
- Goodman J., Weare J., 2010, *Communications in Applied Mathematics and Computational Science*, Vol. 5, 65
- Gough D. O., 1990, in Osaki Y., Shibahashi H., eds, *Lecture Notes in Physics*, Berlin Springer Verlag Vol. 367, Progress of Seismology of the Sun and Stars. p. 283, doi:10.1007/3-540-53091-6
- Gough D. O., 2002, in Battrick B., Favata F., Roxburgh I. W., Galadi D., eds, ESA Special Publication Vol. 485, Stellar Structure and Habitable Planet Finding. pp 65–73
- Gough D. O., Thompson M. J., 1988, in Christensen-Dalsgaard J., Frandsen S., eds, IAU Symposium Vol. 123, Advances in Helio- and Asteroseismology. p. 155
- Grevesse N., Sauval A. J., 1998, *Space Sci. Rev.*, **85**, 161
- Gruberbauer M., Guenther D. B., Kallinger T., 2012, *ApJ*, **749**, 109
- Guenther D. B., Kim Y.-C., Demarque P., 1996, *ApJ*, **463**, 382
- Hacyan S., Dultzin-Hacyan D., Torres-Peimbert S., Peimbert M., 1976, *Rev. Mex. Astron. Astrofis.*, **1**
- Hammer J. W., et al., 2005, *Nuclear Physics A*, **758**, 363
- Herwig F., 2000, *A&A*, **360**, 952

- Hidalgo S. L., et al., 2018, *ApJ*, **856**, 125
- Houdek G., 2004, in Celebonovic V., Gough D., Däppen W., eds, American Institute of Physics Conference Series Vol. 731, Equation-of-State and Phase-Transition in Models of Ordinary Astrophysical Matter. pp 193–207, doi:10.1063/1.1828405
- Houdek G., Gough D. O., 2007, *MNRAS*, **375**, 861
- Iglesias C. A., Rogers F. J., 1996, *ApJ*, **464**, 943
- Imbriani G., et al., 2005, *European Physical Journal A*, **25**, 455
- Jimenez R., Flynn C., MacDonald J., Gibson B. K., 2003, *Science*, **299**, 1552
- Kjeldsen H., Bedding T. R., 1995, *A&A*, **293**, 87
- Kjeldsen H., Bedding T. R., Christensen-Dalsgaard J., 2008, *ApJ*, **683**, L175
- Kunz R., Fey M., Jaeger M., Mayer A., Hammer J. W., Staudt G., Harissopulos S., Paradellis T., 2002, *ApJ*, **567**, 643
- Lebreton Y., Goupil M. J., 2014, *A&A*, **569**, A21
- Lebreton Y., Fernandes J., Lejeune T., 2001, *A&A*, **374**, 540
- Lund M. N., et al., 2017, *ApJ*, **835**, 172
- Maeder A., 1975, *A&A*, **40**, 303
- Marigo P., Girardi L., Bressan A., Groenewegen M. A. T., Silva L., Granato G. L., 2008, *A&A*, **482**, 883
- Mathur S., et al., 2012, *ApJ*, **749**, 152
- Mazumdar A., et al., 2014, *ApJ*, **782**, 18
- Metcalfe T. S., Creevey O. L., Christensen-Dalsgaard J., 2009, *ApJ*, **699**, 373
- Metcalfe T. S., et al., 2012, *ApJ*, **748**, L10
- Metcalfe T. S., et al., 2014, *ApJS*, **214**, 27
- Metcalfe T. S., Creevey O. L., Davies G. R., 2015, *ApJ*, **811**, L37
- Michaud G., Richer J., Vick M., 2011, *A&A*, **534**, A18
- Miglio A., Christensen-Dalsgaard J., di Mauro M. P., Monteiro M. J. P. F. G., Thompson M. J., 2003, in Thompson M. J., Cunha M. S., Monteiro M. J. P. F. G., eds, Proceedings of the Asteroseismology Workshop Vol. 1, Asteroseismology Across the HR Diagram. pp 537–540
- Monteiro M. J. P. F. G., Thompson M. J., 1998, in Deubner F.-L., Christensen-Dalsgaard J., Kurtz D., eds, IAU Symposium Vol. 185, New Eyes to See Inside the Sun and Stars. p. 317
- Monteiro M. J. P. F. G., Thompson M. J., 2005, *MNRAS*, **361**, 1187
- Monteiro M. J. P. F. G., Christensen-Dalsgaard J., Thompson M. J., 1994, *A&A*, **283**, 247
- Monteiro M. J. P. F. G., Christensen-Dalsgaard J., Thompson M. J., 2000, *MNRAS*, **316**, 165
- Morel P., Thévenin F., 2002, *A&A*, **390**, 611
- Nemmen R. S., Gorganopoulos M., Guiriec S., Meyer E. T., Gehrels N., Sambruna R. M., 2012, *Science*, **338**, 1445
- Nsamba B., Campante T. L., Monteiro M. J. P. F. G., Cunha M. S., Rendl B. M., Reese D. R., Verma K., 2018, *MNRAS*, **477**, 5052
- Paxton B., Bildsten L., Dotter A., Herwig F., Lesaffre P., Timmes F., 2011, *ApJS*, **192**, 3
- Paxton B., et al., 2013, *ApJS*, **208**, 4
- Peimbert A., Peimbert M., Luridiana V., 2002, *ApJ*, **565**, 668
- Rauer H., et al., 2014, *Experimental Astronomy*, **38**, 249
- Ribas I., Jordi C., Torra J., Giménez Á., 2000a, *MNRAS*, **313**, 99
- Ribas I., Jordi C., Giménez Á., 2000b, *MNRAS*, **318**, L55
- Richer J., Michaud G., Turcotte S., 2000, *ApJ*, **529**, 338
- Rogers F. J., Nayfonov A., 2002, *ApJ*, **576**, 1064
- Roxburgh I. W., Vorontsov S. V., 2003, *A&A*, **411**, 215
- Seaton M. J., 2005, *MNRAS*, **362**, L1
- Silva Aguirre V., et al., 2013, *ApJ*, **769**, 141
- Silva Aguirre V., et al., 2015, *MNRAS*, **452**, 2127
- Silva Aguirre V., et al., 2017, *ApJ*, **835**, 173
- Sobol I. M., 1967, *USSR Comp. Math. and Math. Phys.*, **7**, 4
- Steigman G., 2010, *J. Cosmology Astropart. Phys.*, **4**, 029
- Tassoul M., 1980, *ApJS*, **43**, 469
- Théado S., Vauclair S., 2001, *A&A*, **375**, 70
- Thoul A. A., Bahcall J. N., Loeb A., 1994, *ApJ*, **421**, 828
- Turcotte S., Richer J., Michaud G., 1998, *ApJ*, **504**, 559
- Ulrich R. K., 1986, *ApJ*, **306**, L37
- Ulrich R. K., 1988, in Christensen-Dalsgaard J., Frandsen S., eds, IAU Symposium Vol. 123, Advances in Helio- and Asteroseismology. p. 299
- Varenne O., Monier R., 1999, *A&A*, **351**, 247
- Vauclair S., 1999, *A&A*, **351**, 973
- Vauclair S., Vauclair G., Schatzman E., Michaud G., 1978a, *ApJ*, **223**, 567
- Vauclair G., Vauclair S., Michaud G., 1978b, *ApJ*, **223**, 920
- Verma K., et al., 2014a, *ApJ*, **790**, 138
- Verma K., Antia H. M., Basu S., Mazumdar A., 2014b, *ApJ*, **794**, 114
- Verma K., Hanasoge S., Bhattacharya J., Antia H. M., Krishnamurthi G., 2016, *MNRAS*, **461**, 4206
- Verma K., Raodeo K., Antia H. M., Mazumdar A., Basu S., Lund M. N., Silva Aguirre V., 2017, *ApJ*, **837**, 47
- Vorontsov S. V., 1988, in Christensen-Dalsgaard J., Frandsen S., eds, IAU Symposium Vol. 123, Advances in Helio- and Asteroseismology. p. 151
- Weiss A., Schlattl H., 2008, *Ap&SS*, **316**, 99
- West C., Heger A., 2013, *ApJ*, **774**, 75
- de Meulenaer P., Carrier F., Miglio A., Bedding T. R., Campante T. L., Eggenberger P., Kjeldsen H., Montalbán J., 2010, *A&A*, **523**, A54

## APPENDIX A: DIFFERENT MEASURES OF THE AMPLITUDE OF THE HELIUM GLITCH SIGNATURE

In principle, we can use any of the four measures of the amplitude discussed in Section 2 for the calibration. In practice, however,  $A_{\text{He}}$  and  $A_{\text{He}}/\Delta_{\text{He}}$  are poorly determined due to the uncertainties in the observed frequencies. Both of these quantities are tightly correlated with  $\Delta_{\text{He}}$ , and the resulting trade-off leads to the large observational errorbar on them. For an example in Figure A1, we show the scatter in  $A_{\text{He}}$ ,  $A_{\text{He}}/\Delta_{\text{He}}$ ,  $A_{\nu_0}$  and  $\langle A_{\nu} \rangle$  as a function of  $\Delta_{\text{He}}$  obtained by fitting the different realizations of 16 Cyg A data using the Method A. The spread along an axis represents the observational uncertainty on the corresponding quantity. Note a factor of 4 variation of  $A_{\text{He}}$  and  $A_{\text{He}}/\Delta_{\text{He}}$  in panels (a-b). The  $A_{\nu_0}$  is also correlated with  $\Delta_{\text{He}}$  for an arbitrary choice of  $\nu_0$ , but its variation is only a factor of 2 in the worse case as seen in panel (c). The correlation changes from being positive to negative as  $\nu_0$  increases, and we can choose a value of  $\nu_0$  which corresponds to approximately zero correlation and get the corresponding most precise  $A_{\nu_0}$ . Instead of determining the most appropriate value of  $\nu_0$  and using the corresponding  $A_{\nu_0}$  for the calibration, we used average amplitude,  $\langle A_{\nu} \rangle$ . As can be seen in panel (d), this choice is better than the choices of  $A_{\text{He}}$  and  $A_{\text{He}}/\Delta_{\text{He}}$  and also  $A_{1600}$  and  $A_{2400}$ , but slightly worse than  $A_{2000}$ .

## APPENDIX B: IMPACT OF THE SURFACE TERM

The observed and best-fitting model frequencies are systematically different due to the differences in the near-surface layers of the star and the model. This difference is known as the “surface term”. The helium ionization zones in the

**Table B1.** Fitted parameters for the corrected model frequencies of 16 Cyg A. The  $\sigma_{\text{stat}}$  is the mean of the negative and positive uncertainties obtained using the Monte-Carlo simulation for the corresponding observed parameter.

(a, b)	Method A					Method B				
	$\langle A_{\text{He}} \rangle$ ( $\mu\text{Hz}$ )	$\Delta_{\text{He}}$ (s)	$\tau_{\text{He}}$ (s)	$\langle A_{\text{CZ}} \rangle$ ( $\mu\text{Hz}$ )	$\tau_{\text{CZ}}$ (s)	$\langle A_{\text{He}} \rangle$ ( $\mu\text{Hz}$ )	$\Delta_{\text{He}}$ (s)	$\tau_{\text{He}}$ (s)	$\langle A_{\text{CZ}} \rangle$ ( $\mu\text{Hz}$ )	$\tau_{\text{CZ}}$ (s)
(-0.0, 4.6)	0.4043	107.34	890.48	0.0732	3022.2	0.4190	105.55	911.28	0.0725	3015.9
(-1.0, 4.6)	0.4035	107.73	889.20	0.0729	3026.4	0.4209	106.05	908.32	0.0721	3019.4
(-2.0, 4.0)	0.4039	107.76	889.52	0.0729	3030.0	0.4220	106.12	908.37	0.0721	3022.9
(-2.0, 5.0)	0.4088	108.51	886.38	0.0730	3030.6	0.4316	106.98	902.26	0.0721	3022.1
(-3.0, 4.6)	0.4098	108.54	886.22	0.0729	3034.6	0.4337	107.07	901.56	0.0720	3025.9
$\sigma_{\text{stat}}$	0.0430	5.89	33.30	0.0158	71.7	0.0395	6.05	27.30	0.0147	71.1

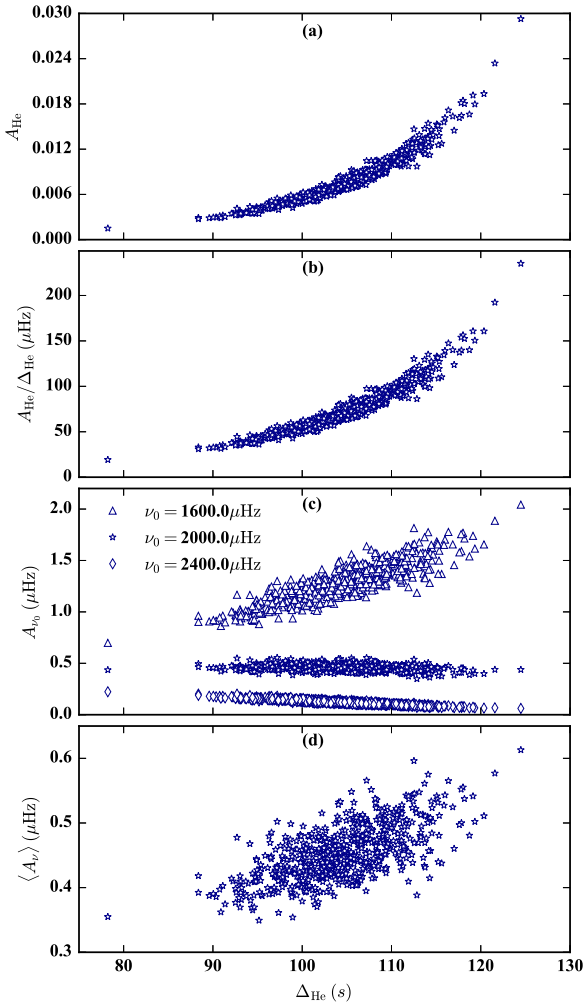


**Figure A1.** Different measures of the amplitude as a function of  $\Delta_{\text{He}}$  for the different realizations of 16 Cyg A data. The three different types of points in panel (c) represent the amplitudes at the three different reference frequencies.

solar-type stars lie deeper where the convection is adiabatically stratified, and hence we can expect 1D stellar models to reproduce these layers. Therefore, the helium glitch signature in the best-fitting model frequencies should reproduce the corresponding observed signature. However, since the observed and best-fitting model frequencies are different, it is not clear while fitting that the additional surface term in

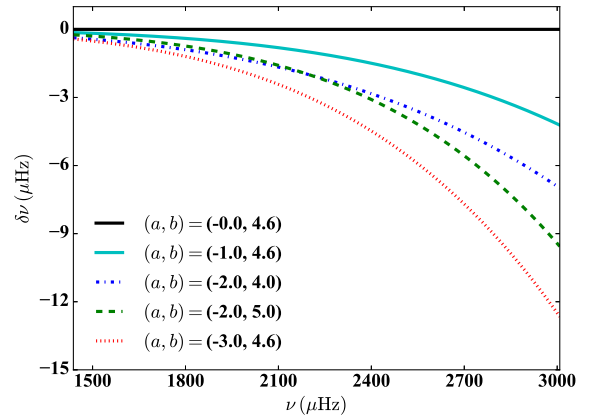


**Figure B1.** Corrections applied to the best-fitting model frequencies of 16 Cyg A. The different lines correspond to the different values of  $a$  and  $b$  (see the text). The horizontal line corresponds to the original model frequencies.

the model frequencies goes completely to the smooth component,  $\nu_{\text{smooth}}$  in case of Method A and  $\delta^2 \nu_{\text{smooth}}$  in case of Method B, without affecting the glitch signatures.

To estimate the effect of the surface term on the glitch signatures, we corrected the best-fitting model frequencies of 16 Cyg A following the power-law correction of Kjeldsen et al. (2008),

$$\delta\nu = a \left( \frac{\nu}{\nu_{\text{ref}}} \right)^b, \quad (\text{B1})$$

where  $a$  and  $b$  are constants, and  $\nu_{\text{ref}} = 2200 \mu\text{Hz}$  is a reference frequency. Figure B1 shows the five different corrections corresponding to the five arbitrary choices of  $a$  and  $b$ . We fitted the resulting frequencies using the Methods A and B, and the fitted parameters are listed in Table B1. Clearly the impact of the surface term is smaller than the impact of the statistical uncertainty on the observed frequencies from the *Kepler* satellite. The reason is that the observational error is a rapidly varying function of the frequency, like the glitch signatures themselves, and interfere with them. On the other hand, since the surface term is a slowly varying function of frequency, it contributes to the smooth component,  $\nu_{\text{smooth}}$  in case of Method A and  $\delta^2 \nu_{\text{smooth}}$  in case of Method B, without affecting the glitch signatures in any significant way.

This paper has been typeset from a  $\text{\LaTeX}$  file prepared by the author.